12-9-2016

Large Eddy Simulation Study of the Effect of Large Wind Farms on Humidity

Oumnia El Fajri

Large eddy simulation study of the effect of large wind farms on humidity

By

Oumnia El Fajri

A Thesis
Submitted to the Faculty of
Mississippi State University
in Partial Fulfillment of the Requirements
for the Degree of Master of Science
in Aerospace Engineering
in the Department of Aerospace Engineering

Mississippi State, Mississippi

December 2016

Large eddy simulation study of the effect of large wind farms on humidity

By

Oumnia El Fajri

Approved:

_____

Adrian Sescu
(Major Professor)

_____

J. Mark Janus
(Committee Member/Graduate Coordinator)

_____

Shanti Bhushan
(Committee Member)

_____

Jason M. Keith
Dean
Bagley College of Engineering

Name: Oumnia El Fajri

Date of Degree: December 9, 2016

Institution: Mississippi State University

Major Field: Aerospace Engineering

Major Professor: Adrian Sescu

Title of Study: Large eddy simulation study of the effect of large wind farms on humidity

Pages in Study: 90

Candidate for Degree of Master of Science

Atmospheric boundary layer flows around wind turbines distributed in a large wind farm can be examined by the use of large eddy simulation (LES), which is based on the assumption that large eddies in the flow are anisotropic and depend on the mean flow and the configuration geometry, while smaller eddies are isotropic and homogeneous, and can be modeled via subgrid scale models. In this thesis, a pseudo-spectral LES code with inflow conditions imposed through a precursor concurrent simulation is utilized to model the flow around a single wind turbine or a large wind farm operating in thermally-stratified conditions. The effect of the wind turbines on humidity is monitored through an additional scalar convection equation. It is found that on average, the effect of an individual wind turbine on the humidity is less than 1%, while the effect of the wind farm on humidity can reach 1-2% in the cumulative wakes.

DEDICATION

I would like to dedicate this thesis to my parents Fatima Araour and Mohamed El Fajri. Thank you for your unconditional love, infinite support and for believing in me. Without you, I would surely not be the person that I am today.

And to my brothers Mohammed Amine El Fajri and Mohamed Anas El Fajri I must say thanks for your encouragement.

ACKNOWLEDGEMENTS

First and foremost, I would like to express my sincere gratitude to my advisor, Dr. Adrian Sescu for his patience, encouragement, excellent support and generous guidance throughout my research work. I would like to thank the committee members Dr. Mark Janus and Dr. Shanti Bhushan for their time and valuable input. I would also like to thank my classmates John Haywood, Vasileos Sassaniss for their help during my graduate studies.

Next, I must say thanks to Brian Houston for being by my side, Nadine Boufous and El Mahdi Akdi for all their moral support along the way, love and for making this past year unforgivable.

Finally, I would like to express my gratitude to Ms. Tamra Hannon Swan for helping me with everything since the first day I came to Starkville.

TABLE OF CONTENTS

LIST OF TABLES

LIST OF FIGURES

CHAPTER I

INTRODUCTION

1.1 Thesis organization

The thesis is structured into five chapters: in chapter 1 an introduction into the field of wind energy and a description of the effect of the wind farms on the environment are included; in chapter 2, a literature review about the atmospheric boundary layer and large eddy simulations is presented; chapter 3 proceeds with the description of the mathematical model and the numerical algorithm utilized to obtain the results. In chapter 4, a description of the simulation cases and various results along with a discussion are included. Finally, chapter 5 outlines the conclusions and provides suggestions in regard to potential future research in the area.

1.2 Introduction

Several countries are looking forward to reduce the polluting type of energy production in favor of sustainable energy. The latter, also called green energy, contributes to the preservation of the environment. Wind energy in particular has a very low environmental impact compared to fossil fuels, since no air pollutant is emitted. The number and size of wind farms are increasing considerably nowadays, and they can be found onshore and offshore across the globe. The 2012 Q3 Report [75] claimed that "U.S" wind power installed capacity supplies 3% of the nation's electricity. In order to be more efficient, they need to be widespread on different geographical areas with high

winds, which motivated different research groups to analyze their potential impact on the communities or on the environment. Studying wind turbines can help achieve a better understanding of the effect that they may have on the atmospheric boundary layer. The purpose of this study is to gain a better understanding about how a large wind farm can influence humidity in the atmosphere. Results from Baidya Roy and Traiteur [7] show that wind farms affect near surface fluxes of heat and momentum.

Because of their size, large wind farms have a direct impact on the atmospheric boundary layer physics and ultimately, on the local weather. Since a large number of wind turbines are in motion, their rotors generate turbulent wakes that contribute significantly to mixing and exchanges of heat and momentum in the vertical direction. Over the years, multiple studies were conducted by different research groups; Taylor [96], Cleijine [25], Jensen et al. [44] and Barthelmie et al. [10] used experimental field measurements, Elliot [32] and Chamorro and Porté-Agel [22] used wind tunnel testing and Barthelmie et al. [11] and Ivanell [42] employed computational fluid dynamics models in order to evaluate and analyze all aspects of the effects of individual wind turbines or wind farms. A case study conducted in Indiana by Henschen et al. [41] suggested that different results are obtained during day and night times; as the wind goes through the turbine rotor, the air temperature and humidity are increased overnight, while the opposite happens during the day. The same conclusion was reached during the Wangara experiment as reported in Clark et al. [24] who found that the level of water vapor in the atmosphere varied with respect to the stratification. But also, with the numerical study included in Baidya Roy et al. [8], where the authors used the Regional Atmospheric Modeling System (RAMS) solver and find out that wind farms slow down

the wind at the turbine hub height, and that the impact of wind turbines on the atmospheric turbulence is more powerful in early hours due to the low level jet that happens during the night.

It is desirable to build numerical tools that will allow scientists and engineers to acquire accurate data and perform rapid predictions of the flow around wind turbines. Numerical studies concerning the flows around wind farms have been proposed and tested over the years. Based on the level of accuracy, numerical models applied to turbulent flows can be broadly classified in Direct Numerical Simulation (DNS), Reynolds Averaged Navier Stokes (RANS) and Large Eddy Simulation (LES). DNS resolves all flow scales from the large eddies that produce most of the energy in the flow to the small eddies that are responsible for dissipation. Because the Reynolds number in the atmospheric boundary layer is very high (in the order of 10^7-10^8), the use of DNS would require an immense mesh implying a large number of degree of freedoms (scaling with $Re^{9/4}$). This exceeds the computational resources that are available today. To solve wake turbulence, the most promising techniques are RANS and LES, but for further deepening in the analysis of anisotropic flows and the swirling regions that exist in the wake, LES is the most suitable technique. In addition, by being the most efficient method to resolve the large eddies in a given flow, LES gives also a trade-off between the cost and storage.

Since the atmospheric boundary layer is an important contributor to the dynamics of the entire atmosphere, it is analyzed in details from many perspectives. Over the last decades, LES has been an important tool, starting with the pioneering study of neutral and unstable boundary layers by Deardorff [28]. He investigated eddy shapes, which

helped to comprehend the mean quantities profile in the ABL. Later LES studies (see, for example, Wyngaard and Brost [103] and Moeng [60], [61]) estimated pseudo-random turbulent structures in time and space and examined the boundary layer turbulence; the models helped in improving turbulence modeling. Atmospheric stability effects on wind farms in Denmark were analyzed by Barthelmie and Jensen [10], where the authors investigated the power loss and efficiency due to the turbine wakes.

In this work, LES simulations are performed to study the effect of large wind farms on humidity budget in the atmospheric boundary layer. An LES code-solving for the incompressible Navier-Stokes equations is employed where the humidity is modeled using an additional scalar convection equation. We consider fully-developed and fully stationary conditions in lateral direction for our wind farm, which is a specific ideal case, since real wind farms can be located on complex terrain and have different behavior depending on their surroundings.

CHAPTER II

ATMOSPHERIC BOUNDARY LAYER

The atmospheric boundary layer (ABL), also known as the planetary boundary layer, is the lowest level of the Earth atmosphere where turbulence is important. ABL can be divided into regions aligned along the vertical direction depending on the local time of the day: the convective mixed layer (unstable boundary layer) can measure between 800m and 1.5 km, residual layer, and stable boundary layer can measure between 300m and 500m. Its properties are entirely influenced by its contact with the ground and thus affects different variables, such as velocity, temperature, or moisture.

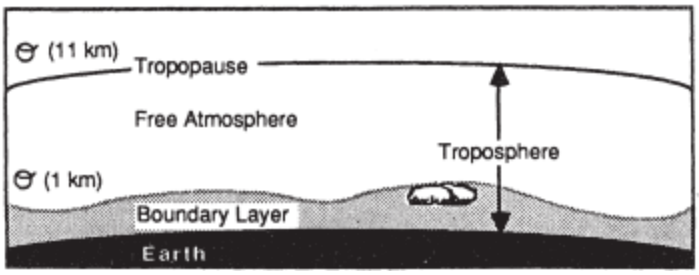

Figure 2.1 Diagram of different layer of the atmosphere from Stull [91]

To be able to study turbulence, we have to consider the flow behavior along both horizontal and vertical directions because different quantities characterize the boundary layer. The vertical direction is dominated by turbulence, which comes in different order of magnitude; it helps the boundary layer to deal with the surface forcing that are

constantly changing. The heat and moisture fluxes are induced by external forcing and can change the boundary layer state. Many types of analysis methods have been directed to study the boundary layer, such as wind tunnel measurements, numerical simulations of turbulence, and theoretical techniques.

The global understanding of the stably-stratified atmospheric boundary layer has been a subject of discussion in numerous books (see, for example, Garratt [33]). Mason and Thompson [54] simulated neutral boundary layers using LES to study the turbulence and the mesh resolution effects on the results. The outcomes from their study showed that the production and loss of turbulent kinetic energy are equal at a certain height. From the experiments performed by Albertson et al. [2], it was shown that the strong gradients in the ABL produce abundant turbulent kinetic energy in consideration of the dissipation. A comparison of the performance in simulating the neutral regime was done by Andrén et al. [5], [4]; the codes used in their study showed the same accuracy from the resolved part, but the results differed in terms of the sub-grid models used. For the stable ABL case, the use of LES was not pertinent at that time due to the damping motion imposed by the gravitational force. This inconvenience did not prevent several researchers to use LES and obtain acceptable results, for example Coleman et al. [26]. Haywood and Sescu [39] studied the interaction between the ABL flow and objects and demonstrated that their effect is directly linked to the key features of the ABL, creating turbulent regions in the ABL. These regions were observed by the experimental work of Augstein et al. [6] in the Atlantic Trade Wind Experiment (ATEX). Other various studies can be enumerated, such as Mason and Derbyshire [55] who performed LES of ABL and made comparisons with field measurements conducted by Derbyshire [31]. In his dissertation, Albertson [1] gave

a literature review that encompasses all major development in both LES and ABL fields. The convective boundary layer, where the largest eddies have sizes in the order of magnitude as the depth of the ABL, was studied by Garratt [33], Sorbjan [87], Panofsky and Dutton [69] and Wyngaard [102].

Wind power is a remarkable alternative renewable energy, experiencing an exceptional growth over the last decades. There are concerns that very large wind farms that are being installed may impact the climate at a regional or even global scale. Exchanges of sensible heat and humidity between the ground and the overlying atmospheric boundary layer may directly impact the near surface atmospheric temperature and moisture. These, in turn, may affect the turbulence levels in the atmosphere and the growth of the atmospheric boundary layer and modify the entrainment of air from above layers. At the global scale, Keith et al. [46] describes a series of simulations using community Global Circulation Models (GCMs) to predict the effects of massive implementations of wind farms. Potential impacts of large wind farms on weather were also explored by Barrie and Kirk-Davidoff [9].

At a smaller scale, Baidya-Roy et al. [8] conducted an analysis of the effect of wind turbine arrays on the local meteorological conditions of a certain region. Crespo and Hernandez [27] performed a more detailed modeling of the turbulence at a smaller scale, using analytical expressions for the turbulent kinetic energy and dissipation rate for the far- and near- wake of the wind turbine. Ivanova and Nadyozhina [43] used a related boundary layer model to calculate the wind and turbulence characteristics inside a wind farm. Meyers and Meneveau [56] performed LES of arrays of wind turbines in the atmospheric boundary layer.

Calaf et al. [19, 20] performed a suite of large eddy simulations of atmospheric boundary layer interacting with a fully-developed wind farm, in which wind turbines are modeled using the classical actuator disk concept in order to quantify the vertical transport of momentum and kinetic energy across the boundary layer. The outcome of these simulations led to the development of a new parameterization of the momentum roughness scale for wind farms. The extension of this parameterization to thermally-stratified conditions was carried out by Sescu and Meneveau [82].

Much insight about the interaction of wind farms and the atmospheric boundary layer has been acquired by combination of wind tunnel experiments, field observations, and numerical simulation studies (Porté-Agel et al. [73, 74], Lu and Porté-Agel [51], Chamorro and Porté-Agel [23], Wu and Porté-Agel [104], Zhang et al. [105], or Smith et al. [79]). In Porté-Agel et al [73], for example, the LES results were validated using experimental data, where three types of models were employed to characterize the rotor-induced forces.

Few studies were focused on monitoring the effect of large wind farms on humidity in the atmosphere or, more importantly, about the effect on the agriculture. Some studies focused on field measurements; one example is the Crop/Wind-energy Experiment (CWEX) [76] performed in 2010 and 2011 in Iowa at a utility-scale wind farm that was installed in the proximity of an agricultural site. Based on some observations, it was concluded that the wakes generated by the wind turbines may delay the dew duration knowing that a high level of dew means more moisture in the air, which would suggest that wind farms decrease the near-surface humidity. This has not been verified numerically. One of the objectives of this research is to determine the effect of

individual wind turbines or wind farms on humidity using large eddy simulations with low-order modeling (actuator disk model) of the rotor disk forcing.

CHAPTER III

LARGE EDDY SIMULATION

LES is an important tool in turbulence research, and it has several benefits compared to RANS or DNS technique it is more accurate than the former and less computational demanding than the latter. LES relies on the hypothesis that most of the energy of the flow is contained in the large scales of turbulence, while the low scales tend to be isotropic. This suggests that the large scale structures must be resolved by the numerical method, while the low scale structure need to be modeled using various subgrid scale modeling methods. Since the Reynolds number in the ABL is very large, the use of DNS would become very expensive (beyond the reach of today's computational resources). LES combined with wall modeling; however, is a promising tool, and it was found that it provides a reasonable comprehension of wind farm aerodynamics and their physics (see Mehta et al. [57]).

In LES, the large eddies depend on the gross flow characteristics and are resolved, while the smaller ones are modeled in terms of resolved scales of motion. Because of the incomplete solution, the equations must be modified since the cascading energy would have a different outcome. Depending on the level of accuracy, different types of eddies are resolved by LES: the large eddies that transport most of the flow's energy and not influenced by the molecular viscosity, and the intermediate ones that are not influenced by the large scales and boundary conditions. The smaller eddies, which are not resolved

by the numerical method, are modeled using subgrid scale models (SGS). LES can be split into two classes depending on the way the subgrid scale is approached: implicit LES which uses the numerical dissipation to deal with the SGS (Sagaut [77] and Grindstein et al. [36]); and explicit LES that includes an explicit SGS model (the original Smagorinsky model is one of the simplest explicit SGS model). All large eddies that fall in the LES resolved range of analysis are covered by the grid, which suggest a spatial filtering of the Navier Stokes equations in order to remove the unresolved scales. In the next section, the LES framework that is applied in this work is described.

Using a pseudo spectral finite difference LES code, Moeng [61] simulated the convective flow in the ABL and compared the outcome with the experimental data. In a later study, Wyngaard and Brost [104] investigated the vertical profiles of a scalar transported by the wind using LES. It gave insight into the scalar variance relation to the surface flux. Other researchers used the LES methodology proposed by Moeng (see for example Hechtel et al. [40]) to investigate the effect of nonhomogeneous temperature at the surface boundary on the mixed layer. Hadfield et al. [37] found that the mean horizontal wind is capable of diminishing the circulation. Nieuwstadt [66] and van Haren and Nieuwstadt [97] work had a significant implication on the comprehension of the transport of water vapor at the earth's surface. Schumann [81] used large eddy simulation to investigate the turbulent transport of nonreactive and reactive species in the convective ABL and found that diffusivity is dependent on the buoyancy. In another work, Schmidt and Schumann [79] examined the coherent structures in the unstable atmospheric boundary layer. Sorbjan [88] examined the convective boundary layer growth using an LES code. The same applies to Mason's work [53], where not only the convective

boundary layer was studied, but also the mesh characteristics (size of the domain, mesh resolution) effects on the simulation outcomes. Different LES results obtained by different research groups have been compared in Andrén et al. [5] in order to address the differences and the accuracy among them. Aforementioned studies only considered the flat terrain; several researchers studied wavy terrain surface effects on the atmospheric boundary layer. Schumann [81] showed that the length scales associated with vertical velocity and velocity variance are not influenced by the wavy aspect of the land surface. Walko et al. [100] investigated how the convective atmospheric boundary layer is affected by hilly terrain. Shaw and Schumann [84] studied the ABL within a forest using LES to understand regional scale surface fluxes behavior.

3.1 Governing equations

Navier-Stokes equations are derived from the conservation principles of mass, momentum and energy and in the most general case they describe the motion of a compressible, Newtonian fluid. In this thesis, the incompressible version of Navier-Stokes equations is utilized after a filter was applied to remove the small scales of turbulence that is not resolved by the grid:

$$\frac{\partial \tilde{u}_i}{\partial x_i} = 0 \tag{3.1}$$

$$\frac{\partial \tilde{u}_i}{\partial t} + \tilde{u}_j \frac{\partial \tilde{u}_i}{\partial x_j} = -\frac{\partial \tilde{p}^*}{\partial x_i} - \frac{\partial \tilde{\tau}_{ij}}{\partial x_j} + \delta_{i3} g \frac{\tilde{\theta} - \langle \theta \rangle}{\theta_0} + f_c \varepsilon_{ij3} \left(\tilde{u}_j - u_{gj} \right) + F_i \tag{3.2}$$

$$\frac{\partial \tilde{\theta}}{\partial t} + \tilde{u}_j \frac{\partial \tilde{\theta}}{\partial x_j} = -\frac{\partial \pi_i^{\theta}}{\partial x_i} + F_{\theta} \tag{3.3}$$

$$\frac{\partial \tilde{q}}{\partial t} + \tilde{u}_j \frac{\partial \tilde{q}}{\partial x_j} = -\frac{\partial \pi_i^{q}}{\partial x_i} \tag{3.4}$$

where the tilde ˜ and the angle brackets ⟨ ⟩ represent the spatial filtering and the horizontal average, respectively; $\tilde{u}_i$ is the velocity vector field with components in the streamwise direction, lateral direction, and vertical direction; $\tilde{\theta}$ and θ_0 are the resolved potential temperature and the reference temperature, respectively; f_c is the Coriolis parameter; g is the gravitational acceleration; δ_{ij} is the Kronecker delta; $\tilde{p}^*$ is the effective pressure divided by reference density; ε_{ijk} is the alternating unit tensor; F_θ is the temperature forcing term; F_i is a forcing term modeling the effect of the wind turbines. The subgrid-scale (SGS) stress, heat and humidity fluxes:$\tau_{ij}=\widetilde{u_i u_j}-\tilde{u}_i\tilde{u}_j$, $\pi_j^{\theta}=\widetilde{u_j\theta}-\tilde{u}_j\tilde{\theta}$, $\pi_j^{q}=\widetilde{u_j q}-\tilde{u}_j\tilde{q}$, are modeled via the Lagrangian scale-dependent SGS model as developed by Bou-Zeid et al. [15] where the required averages are accumulated in time. The scale-dependent Lagrangian model was shown to have good dissipation characteristics. The Reynolds number is very large in the atmospheric boundary layer, therefore the flow at the ground is modeled using the Monin-Obukhov similarity theory Monin and Obukhov [64] and Obukhov [67]; because of the magnitude of the Reynolds number, the molecular viscous diffusion term in the momentum equation is neglected.

In LES equations, a division into solved and unsolved parts of the dependent variables is made because the grid resolution is not capable of resolving all the turbulence scales in the atmosphere. The unresolved part includes the small-scale fluctuations only, while the solved part includes the mean and large-scale fluctuations. By applying a filter to the original incompressible Navier-Stokes equations, we separate the resolved part from the unresolved one Leonard [49], Aldama [3] or Pope [71].

In order to evaluate the potential temperature (θ) and humidity (q), the LES equations also include the transport equations of these two scalars:

$$\partial_0 S + U_j \partial_j S = D^S \partial_j \partial_j S \tag{3.5}$$

where D^S is the constant molecular diffusivity of scalar S in air. The filtering process was applied here again to obtain the transport of the resolved scalar field.

3.2 Subgrid Scale Modeling

In this section, a brief discussion of the SGS models that are based on the original eddy-viscosity Smagorinsky model is included. Turbulence simulation and modeling are extremely important for aerodynamic and fluid dynamics applications, and SGS modeling within LES makes no exception. A comprehensive description of the SGS modeling is given in the article of Meneveau [58]. As discussed previously, the range of small scales in the fluid motion cannot be resolved by the governing equations; as a result, the use of subgrid scale modeling is necessary because the effects of these unresolved small eddies are taken into account through additional energy dissipation terms in the governing equations. To this end, a filtering is applied to the Navier-Stokes equations Leonard [49], which separates the large and small scales. Since the small scales introduce additional unknowns in the equations, modeling is required to link them to the other flow variables. Next, several SGS models are discussed, starting with the simplest one and finishing with the most complex.

3.2.1 Smagorinsky model

This model is the first eddy-viscosity type model as introduced by Smagorinsky [85], and it is considered the most popular and most efficient SGS model. It continues to

be used because of its effective energy transfer technique going from large scales to smaller scales until the energy dissipates into the viscous scales. Deardorff [29], as mentioned before, was the pioneer in the turbulence and eddies investigation. For the purpose of his research, he used Large Eddy Simulation proposed by Smagorinsky. All the following SGS models take origin and are based on the Smagorinsky model. The model was first introduced by Smagorinsky [85] in the framework of modeling the atmospheric turbulence, and it is based on the concept of mixing length; according to this model, the SGS stress tensor is represented as follow:

$$\tau_{ij}^{SMAG}=-2\nu_T\tilde{S}_{ij}=-2\left(c_{S,\Delta}\Delta\right)^2|\tilde{S}|\tilde{S}_{ij} \tag{3.6}$$

where ν_T is the eddy viscosity, Δ is the filter width, $|\tilde{S}|=\sqrt{2\widetilde{S_{ij}}\widetilde{S_{ij}}}$ is the strain-rate magnitude, $\widetilde{S_{ij}}=0.5(\delta_j\tilde{u}_i+\delta_i\tilde{u}_j)$ is the resolved strain rate tensor and $c_{s,\Delta}$ is the Smagorinsky coefficient, a non-dimensional parameter. Because, the Smagorinsky coefficient (C_s) depends on the boundary conditions and grid mesh aspect ratio, a version involving wall damping functions was proposed by Mason and Thompson [54]. However, in his paper Lilly [50] concluded that the constant C_s=0.17 which was found to be accurate for isotropic turbulence. Other scholars employed different values, such as Deardorff [29], who used C_s=0.1. The variation of the Smagorinsky parameter from one application to the other by different authors revealed some drawbacks of the classical model. Multiple papers noted the deficiencies of this model and these limitations were also verified through experimental studies Tao et al. [95]. In Moin et al. [63], the authors discussed some of the defects that were encountered while using the model such as:

1. The optimal C_s is variable for the different types of turbulent flows, since it is only an a priori parameter.
2. The model is over dissipative close to the solid wall and the eddy viscosity does not fade in a laminar flow.
3. The model does not account for backscatter of energy from small scales to large scales.
4. The model excludes compressibility effects.

By recognizing the shortcoming of Smagorinsky model, scholars developed new models that are more accurate and encompass complex flow characteristics. Various papers showed the contrast between these eddy viscosity SGS models for various applications; Bou-Zeid et al. [14] compared them for flows around rough walls, while Ma et al. [52] made this type of comparison for turbulent flows in water turbine. Andrén et al. [5] performed the same investigations to confirm these deficiencies.

3.2.2 Dynamic model

Over the years, various versions of the eddy-viscosity Smagorinsky model were proposed to avoid the deficiencies of the original model. The dynamic Smagorinsky model was introduced by Germano et al. [34]; this new model was identified as a significant improvement, as it addressed some of the most important Smagorinsky model limitations. In the dynamic model, the Smagorinsky coefficient is determined from the smallest resolved scales. To show this we define:

$$L_{ij}=T_{ij}-\tilde{\tau}_{ij}=\widetilde{\tilde{u}_i\tilde{u}_j}-\tilde{\tilde{u}}_i\tilde{\tilde{u}}_j \tag{3.7}$$

where $T_{ij}=\widetilde{\tilde{u}_i\tilde{u}_j}-\tilde{\tilde{u}}_i\tilde{\tilde{u}}_j$ corresponds to the stress at a test filter scale $\overline{\Delta}=2\Delta$, L_{ij} is the resolved stress tensor, $\tilde{\tau}_{ij}=-2(c_{s,\Delta}\Delta)^2\widetilde{|\tilde{S}|\tilde{S}_{ij}}$, $T_{ij}^{D}=-2\left(c_{s,\overline{\Delta}}\overline{\Delta}\right)^2\overline{|\tilde{S}|\,\tilde{S}_{ij}}$, $\alpha=2$ the superscript, D

expresses the deviatoric (trace free) part of the tensor; if we replace it in L_{ij}equation, it will generate the error from the use of the Smagorinsky model:

$$e_{ij}=L_{ij}^{D}-\left(T_{ij}^{D}-\tilde{\tau}_{ij}\right)=L_{ij}^{D}-c_{s,\Delta}^{2}2\Delta^{2}[\widetilde{|\bar{S}|\bar{S}_{ij}}-4\frac{c_{S,2\Delta}^{2}}{c_{s,\Delta}^{2}}\widetilde{|\bar{S}|}\widetilde{\bar{S}_{ij}}]=L_{ij}^{D}-c_{s,\Delta}^{2}M_{ij} \quad (3.8)$$

where $M_{ij}=2\Delta^{2}[\widetilde{|\bar{S}|\bar{S}_{ij}}-4\frac{c_{S,2\Delta}^{2}}{c_{s,\Delta}^{2}}\widetilde{|\bar{S}|}\widetilde{\bar{S}_{ij}}]$ and $c_{s,\Delta}^{2}=\frac{<L_{ij}M_{ij}>}{<M_{ij}M_{ij}>}$

This model has its disadvantages as well. Vreman et al. [99] raised an important question about the values modification of the Smagorinsky coefficient; they found that the sign of the coefficient has a great importance for the dissipation of kinetic energy, which assumes only positive values. Ghosal et al. [35] proposed a new version of the dynamic model that rectifies the utility of the model and broadens its application to inhomogeneous flows.

The dynamic model is suitable for flow domains with at least one homogenous direction, because it involves spatial averaging along these directions. This makes the model ineffective when complex geometries are involved. To deal with this issue, wall adapting local eddy viscosity model (WALE) was developed by Nicoud and Ducros [65] for complex geometries. The planar-averaged scale-dependent dynamic model was used when the scale dependence parameter was measured where $c_{s,\Delta}^{2}=\frac{<Q_{ij}N_{ij}>}{<N_{ij}N_{ij}>}$, $Q_{ij}=\widehat{\tilde{u}_{i}\tilde{u}_{j}}-\hat{\tilde{u}}_{i}\hat{\tilde{u}}_{j}$

and $N_{ij}=2\Delta^{2}[\widetilde{|\bar{S}|\bar{S}_{ij}}-16\frac{c_{S,2\Delta}^{2}}{c_{s,\Delta}^{2}}\widetilde{|\bar{S}|}\widetilde{\bar{S}_{ij}}]$.

A very interesting approach was proposed by Meneveau et al. [59] who introduced an alternative Lagrangian averaged scale invariant SGS model. Here, the averaging is performed in time by following the fluid streamline. This model is a great substitute of the preceding models, since it can be applied for heterogeneous flows while

having the same advantages; it also shows Galilean invariance. Within this model, the weighted time average can be represented as following:

$$E= \int_{-\infty}^{t} e_{ij}[z(t'),t']e_{ij}[z(t'),t']W(t-t')dt' \tag{3.9}$$

where z (t') are the precedent positions of the fluid elements, W(t) is a relaxation function. Then, we can obtain the coefficient by varying E in function of $c_{s,\Delta}^2$:

$$\frac{\partial E}{\partial c_{s,\Delta}^2} = \int_{-\infty}^{t} 2e_{ij} \frac{\partial e_{ij}}{\partial c_{s,\Delta}^2} W(t-t')dt'=0 \tag{3.10}$$

$$c_{s,\Delta}^2 = \frac{\int_{-\infty}^{t} L_{ij}M_{ij}[z(t'),t']W(t-t')dt'}{\int_{-\infty}^{t} M_{ij}M_{ij}[z(t'),t']W(t-t')dt'} = \frac{J_{LM}}{J_{MM}} \tag{3.11}$$

Other manipulations have been proposed in the literature in order to obtain the relaxation transport equations. An example of application of this model in complex domains is Haworth et al. [38] who used the model to investigate flows inside combustion engines.

3.2.3 Scale dependent dynamic model

Porté-Agel et al. [74] developed the scale dependent dynamic model (SDDM) and implemented it in a LES framework of neutral atmospheric boundary layer. This model corresponds to an improvement of the dynamic model proposed by Germano by overcoming some of its drawbacks. SDDM approach is based on adding a second scale test filtering which gives the advantage of evaluating dynamically the coefficient from the simulation, while the scale varies as a function of the resolved flow, without requiring any parameters regulation.

Bou-Zeid et al. [15] introduced the Lagrangian dynamic model with the scale dependent parameterization, which is a combination of two existing ones. This model showed a significant improvement in simulation results. The general approach consists of

the first and second test filtering operations with the implementation of the coefficient dynamically. Because the Lagrangian averaging method is known to be slightly more expensive, an easier method has been formulated by introducing a series of manipulations in order to accommodate the test filter scale and by taking into account the coefficient sensitivity near the wall. Using the same idea for the planar averaged coefficient we have:

$$c^2_{s,\Delta}=\frac{<L_{ij}M_{ij}>/<M_{ij}M_{ij}>}{(\frac{<Q_{ij}N_{ij}><M_{ij}M_{ij}>}{<N_{ij}N_{ij}><L_{ij}M_{ij}>})}$$

In this thesis, the scale dependent Lagrangian dynamic model plus scalar parameterization is employed, in order to obtain more accuracy for the results. We refer to the works of Stoll et al. [90] and Calaf et al. [20] here since they described this SGS model with some details. The SGS scalar flux is represented as follow:

$$r_i=-\frac{\nu_{SGS}}{Pr_{sgs}}\partial_i\tilde{\theta}=-\frac{C^2_{s,\Delta}\Delta^2|\tilde{S}|}{Pr_{sgs}}\partial_i\tilde{\theta}=-D^2_{s,\Delta}\Delta^2\left|\tilde{S}\right|\partial_i\tilde{\theta} \tag{3.12}$$

where Δ is the filtering length scale, $\left|\tilde{S}\right|$ and $\widetilde{S_{ij}}$ were previously defined in the Smagorinsky model; $\tilde{\tau}_{ij}=2(c_{s,\Delta}\Delta)^2\widetilde{\left|\tilde{S}\right|\tilde{S}_{ij}}$; $D_{s,\Delta}$ is evaluated using the Scale dependent Lagrangian dynamic model. We get therefore the resolved scalar flux as follow:

$$K_i=\widetilde{\tilde{u}_i\tilde{\theta}}-\tilde{\tilde{u}}_i\tilde{\tilde{\theta}}=R_i-\tilde{r}_i \tag{3.13}$$

with $R_i=-D_{s,2\Delta}(2\Delta)^2\widetilde{\left|\tilde{S}\right|\partial_i\tilde{\theta}}$ being the SGS scalar flux at scale 2Δ and $\tilde{r}_i=-D_{s,\Delta}\Delta^2\widetilde{\left|\tilde{S}\right|\partial_i\tilde{\theta}}$

An error can be deduced from the previous equation:

$$e_i=K_i-(R_i-\tilde{r}_i)=K_i-D^2_{s,\Delta}X_i=K_i-D^2_{s,\Delta}\Delta^2[\widetilde{\left|\tilde{S}\right|\partial_i\tilde{\theta}}-4\frac{D_{s,2\Delta}}{D_{s,\Delta}}\widetilde{\left|\tilde{S}\right|\partial_i\tilde{\theta}}] \tag{3.14}$$

It is also assumed that: $\beta=\frac{D_{s,2\Delta}}{D_{s,\Delta}}=1$, thus

$$D^2_{s,\Delta}=\frac{\int_{-\infty}^{t}K_iX_i[z(t'),t']W(t-t')dt'}{\int_{-\infty}^{t}X_iX_i[z(t'),t']W(t-t')dt'} \tag{3.15}$$

3.3 Boundary conditions

The governing equations depend on the initial and boundary conditions. We assume that there is horizontal homogeneity of turbulence in the atmospheric boundary layer in the lateral direction, thus periodic boundary conditions are employed. In the streamwise direction, a precursor concurrent simulation method is applied to impose an inflow condition (Stevens et al. [89], Haywood and Sescu [39]); this precursor method will be explained in details in the section 3.5.

At the top surface, we assume that the vertical gradients of velocity and scalars, and the vertical component of velocity are zero. For the simulations of the convective atmospheric boundary layer dynamics, a capping inversion layer is imposed at the top portion of the domain. A generic equation with the damping term is $\delta_t\phi = \mathcal{L}(\phi) + r(z)\,(\phi - \langle\phi\rangle)\,H(z-z_b)$ where $\mathcal{L}()$ is a spatial differential operator, ϕ is a prognostic variable, $H(x)$ is Heaviside step function, and z_b is the elevation where the sponge layer starts. The relaxation term $r(z)\,(\phi-\langle\phi\rangle)$ dampens fluctuations at time scales larger than a prescribed relaxation time scale $\tau = \frac{1}{r}$; this was demonstrated in Sorbjan [88]. In this work, the relaxation function is given as $r(z) = r_0/2\{1-\cos[\pi(z-z_b)(z_t-z_b)]\}$, where r_0 is a given relaxation constant of order of $0.01s^{-1}$, and z_b indicates the top of the computational domain.

At the bottom surface, the Monin-Obukhov similarity theory is utilized, which can model the flow near the boundary but also the fluxes near it, such as the instantaneous wall stress, in the form:

$$\tau_{i3}|_{z=0} = -u_*^2 \frac{\tilde{u}_i}{V_f} = -\left[\frac{\kappa V_f}{\ln\left(\frac{z}{z_0}\right) - \Psi_M}\right]^2 \frac{\tilde{u}_i}{V_f} \text{ with } \quad i=1,2 \qquad (3.16)$$

$\tau_{13}|_{z=0}$ and $\tau_{23}|_{z=0}$ are the instantaneous local wall stress components, u_* is the friction velocity, z_0 is the effective roughness length, κ=0.4 is the von Karman constant, Ψ_M is the stability correction function for momentum, and $V_f = [\widetilde{u_1}(\Delta z/2)^2 + \widetilde{u_2}(\Delta z/2)^2]^{0.5}$ is the local filtered horizontal velocity at the first vertical level in the grid. The surface heat flux is computed as

$$\langle w'\theta' \rangle_{z=0} = \frac{u_* \kappa (\theta_s - \tilde{\tilde{\theta}})}{\ln\left(\frac{z}{z_{0s}}\right) - \Psi_H} \quad (3.17)$$

where θ_s is the imposed surface potential temperature, $\tilde{\theta}$ denotes the resolved potential temperature at the first vertical level, z_{0s} is the roughness length for scalar (its value is $0.1z_0$), $\Psi_H(\varsigma) = \int_0^{\varsigma} [1 - \phi_H(\varsigma')d\varsigma'/\varsigma']$ is the stability correction function for heat flux ($\varsigma = z/L$) , and ϕ_H is given as $\phi_H(\varsigma) = Pr_t + \beta\varsigma$ where the Prandtl number Pr_t=0.74 , β=5 for stable conditions and $\phi_H(\varsigma) = Pr_t(1-\gamma\varsigma)^{-0.5}$ where γ=16 for unstable conditions.

Due to the injection and extraction of heat coming and leaving the surface layer, it is difficult to keep the horizontal averaged temperature profile stationary. Therefore, a source of heat above the atmospheric boundary layer is imposed in the top portion of the ABL (z=300m) to keep a prescribed thermal stratification Sescu and Meneveau [82] have discussed in details this control algorithm in their paper. The added term is described as follow: $F_\theta = S(x_3,t)[H(x_3 - x_{3b}) - H(x_3 - x_{3t})]$ where H(x) is Heaviside step function, the subscript t and b are the top and bottom of the region where we applied the heat source, the heat source $S(x_3, t+m\Delta t) = S(x_3,t) + U(x_3,t)$ and $U(x_3,t)$ is the PI controller.

3.4 Wind Turbine Parameterization

Due to grid requirements and the computational cost involved, the details of the flow around wind turbines cannot be directly solved by the LES. Therefore, proper parameterizations of the wind turbine must be employed consisting of simplified models that describe the effect of the turbine thrust on the atmospheric flow. The wind turbine parameterization is very important since it will provide us with more knowledge about wakes and their effect on the ABL. There are different types of models: actuator disk model, actuator disk model with rotation and actuator line model. Over the years, various studies have focused on wind turbine wakes; to enumerate few, Crespo and Hernández [27] investigated the effect of atmospheric turbulence on wind turbines wakes and compared their results with experimental data; Vermeer et al. [98] were interested in the farness fading process of the wake and its effect on the turbines, and Chamorro and Porté-Agel [22] used wind tunnel measurements to study the wind turbine wake.

Next, we need to understand the turbine model and how it modifies the flow and creates a wake. Several researchers used the actuator disc principle where the energy and momentum are evaluated through a control volume approach that consists of a tube that includes the disk. This theory has been introduced by Lanchester [47] and further developed for wind turbines by Betz [13] afterwards.

Okulov and van Kuik [68] explained in their paper the efficiency of an ideal wind turbine and introduced the idea that the load on the wind turbine rotor can be represented by a pressure distribution. This approach has been used, for example, by Jimenez et al. [45], where the authors investigated the spectral coherence of turbulence in the wake and in Calaf et al. [19], [20]. According to the actuator disk method, the total drag force

acting on the flow in the streamwise direction is spread across the disk region on all grid points and is represented as follows:

$$F_t=-0.5\rho C_T U_\infty^2 \frac{\pi}{4} D^2 \tag{3.18}$$

where D is the rotor diameter, C_T is the thrust coefficient and $U_\infty$is the upstream velocity. It would be correct to use U_∞ for the case of a singular wind turbine since there can be no interaction or perturbation with other wind turbines. Nevertheless, another equivalent formulation that can be used in case of a large number of wind turbines, such as in a wind farm, should be established which takes into account the drag disk approach.

$$U_\infty=\frac{U_d}{(1-a)} \tag{3.19}$$

where a is called the induction factor. We will rewrite the total thrust force with velocity average because of the interaction of the wind turbine blades and the fluid; the thrust force is, therefore, as follow:

$$F_t=-0.5\rho C'_T \langle \widetilde{u^T} \rangle_d^2 \frac{\pi}{4} D^2 \tag{3.20}$$

where $\langle \tilde{u}^t \rangle_d$ is the averaged time filtered disk velocity and $C'_T=\frac{C_T}{(1-a)^2}$.

We will refer to the literature for the thrust coefficient values: Burton et al. [16] proposed C_T=0.75 and a= 0.25, giving $C'_T=\frac{4}{3}$. In our work, we will be using different values for C'_T in order to compare between the cases.

3.5 Numerical Algorithm

In the present study, the numerical tool is based on the LES code originally developed by Albertson [1] at John Hopkins University, and extensively used in various papers, such as Calaf et al. [19], Calaf et al. [20] and Sescu and Meneveau [82]. The

domain is represented by a box where all side faces have either inflow-outflow or periodic boundary conditions, the top of the box has a zero gradients of velocity and scalars, and at the bottom of the box the Monin-Obukhov similarity theory is applied.

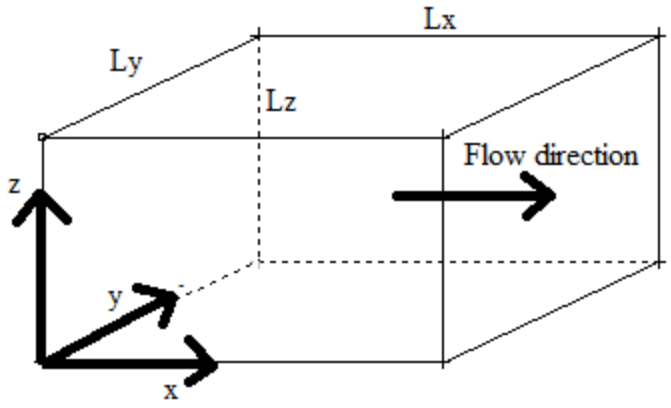

Figure 3.1 Atmospheric Boundary Layer domain

A Cartesian uniformly-spaced grid is considered owing to the wall modeling used at the ground modeling (the viscous dissipation is not resolved but modeled).

$$ {}^{d}\Delta x=\frac{L_x}{N_x} \ , \ {}^{d}\Delta y=\frac{L_y}{N_y} \ , \ {}^{d}\Delta z=\frac{L_z}{N_z-1} \tag{3.21} $$

In the vertical direction, a staggered grid is considered, where different variables are stored on different locations: the vertical velocity component is shifted half a location (grid point) up; it is principally used for incompressible flows. By applying it, we will avoid the discretization errors due to velocity-pressure decoupling.

This is a convenient way since we are using a second order accurate finite centered difference in the vertical direction because of non-periodic boundary conditions in the vertical direction.

In the horizontal directions, we use a pseudo spectral method that involves Fast Fourier Transform (FFT); details of this method are given in Canuto et al. [21]. The following x and y partial derivatives are applied for all variables that we will name (α):

$$\frac{\partial \tilde{\alpha}_i(x,y,z)}{\partial x} = \sum'_{k_x} \sum'_{k_y} [\tilde{\alpha}_i(k_x,k_y,z)(ik_x)] e^{i(k_x x + k_y y)} \tag{3.22}$$

$$\frac{\partial \tilde{\alpha}_i(x,y,z)}{\partial y} = \sum'_{k_x} \sum'_{k_y} [\tilde{\alpha}_i(k_x,k_y,z)(ik_y)] e^{i(k_x x + k_y y)} \tag{3.23}$$

For the vertical direction (z), since they are not homogeneous, we will use a finite centered difference for the derivatives. We will apply it for all variables as well (α):

$$\frac{\partial \widetilde{\alpha_i}}{\partial z}(x,y,z) = \frac{\widetilde{\alpha_i}(x,y,z + \frac{\Delta z}{2}) - \widetilde{\alpha_i}(x,y,z - \frac{\Delta z}{2})}{\Delta z} \tag{3.24}$$

In the pseudo spectral method, aliasing may occur because of the difference between discrete and continuous Fourier coefficients. These errors that appear mainly in the nonlinear convective terms (momentum and scalars) are readjusted with the zero-padding 3/2 rule as explained in Canuto et al. [21].

A precursor simulation is used in the streamwise direction in order to apply realistic turbulent inflow conditions. In this thesis, we use the concurrent precursor method that was first introduced by Stevens et al. [89] in the context of wind farms and further applied it for flows around a box by Haywood and Sescu [39]. The principle of the concurrent precursor method is to run two simultaneous simulations at the same time: wind turbines are included in one flow domain that is called the main simulation, and the other simulation (termed precursor) considers the free atmosphere. Variables in a section from the precursor simulation are blended into the main simulation.

For the time advancement, an Adams-Bashforth method is used, which is an explicit multistep method. The scheme is given as follows:

$$A^{t+\Delta t}=A^{t}+\Delta t\left[\frac{3}{2}\widetilde{g^{t}}-\frac{1}{2}g^{t-\Delta t}\right] \tag{3.25}$$

The pressure variable is determined by solving a Poisson equation to preserve the divergence-free condition for the velocity field.

CHAPTER IV

RESULTS AND DISCUSSION

4.1 Simulation cases

In terms of wind turbines arrangements, two main LES cases are considered: a single wind turbine in the streamwise direction and a wind farm (consisting of 4x4 turbines). It must be mentioned that the case with a single wind turbine in the actual flow domain is in fact an infinite row of turbines in the y-direction, while the case with 4x4 turbines represents four infinite rows of turbines because periodic boundary conditions are used in the y-direction. For each of these 2 cases, 8 and 6 sub-cases are considered, respectively, where 2 parameters are varied: the thrust coefficient (C'_T) that corresponds to $C_T' = \frac{4*b}{1-b}$ where b=0.16 or b=0.333 and the wind velocity (U_g). The following tables enumerates and summarizes all the LES cases where ST stands for “Single Turbine” and WF for “Wind Farm.”

Table 4.1 LES cases for a single wind turbine

Cases	C'_T	U_g (m/s)
ST1	0.761	6
ST2	0.761	8
ST3	0.761	10
ST4	0.761	12
ST5	1.997	6
ST6	1.997	8
ST7	1.997	10
ST8	1.997	12

Table 4.2 LES cases for a (4x4) wind farm

Cases	C'_T	U_g (m/s)
WF1	0.761	6
WF2	0.761	8
WF3	0.761	10
WF4	1.997	6
WF5	1.997	8
WF6	1.997	10

The number of grid points in the three spatial directions are N_x=128, N_y=64, N_z=96. The grid spacing is constant from top to bottom and along the vertical direction

because at the wall, the Monin-Obukhov similarity theory is applied as the wall model, and no grid clustering is required. Along the horizontal directions, the spacing is constant as well because the equations are discretized using the pseudo spectral method. The hub height is located at Z_h=100m from the ground, and the wind turbine diameter is the same for all LES cases configuration, D=100 m. The thermal stratification for all cases is $\Delta\theta=\theta_t-\theta_s$ =0.4, where θ_s is the ground surface temperature and θ_t is the temperature at the top of the atmospheric boundary layer. In the case of the wind farm, the spacing between wind turbines is S_x=1256.6 m for the longitudinal distance and S_y=392.5 m for the lateral distance.

4.2 Single wind turbine

The domain for the single wind turbine is a rectangular box measuring 2000m in the streamwise, 500m in the spanwise and 400m in the vertical direction. The wind turbine is located at 250m in the y direction and 300m in the x direction. Two values of thrust coefficient associated with the wind turbine rotors (1.997 and 0.333) and four values of the wind velocity (6, 8, 10 and 12 m/s) are considered. For the stable stratification conditions considered in this study, the code was running for six physical hours to allow the flow to fully develop.

Figures 4.1 and 4.2 represent contour plots of the instantaneous velocity through z=100m horizontal section for a single wind turbine with thrust coefficient Ct=1.997 and for the different velocities. These contour plots show the wake developing in the downstream of the rotor (the blue region); the spatial extent of the wake seems to increase with velocity, and all parts of the figure show that the wake dissipates in the

downstream. We can also remark that for higher velocities (U=10m/s and U=12m/s), more turbulence is visible through the wiping motion of the wake that releases the vortices. The same idea can be deduced from the contour plots along the y direction that are shown in Figure 4.2. We can remark that below the wind turbine location there is an area of high velocity fluid that gets pinched back into the wake, above the wind turbines we can remark especially for lower velocities cases (6m/s and 8m/s) the flow above the wind turbine going into the upper atmosphere where it will experience mixing. We can see bigger structures in the far wake for lower velocities U=6m/s and U=8m/s.

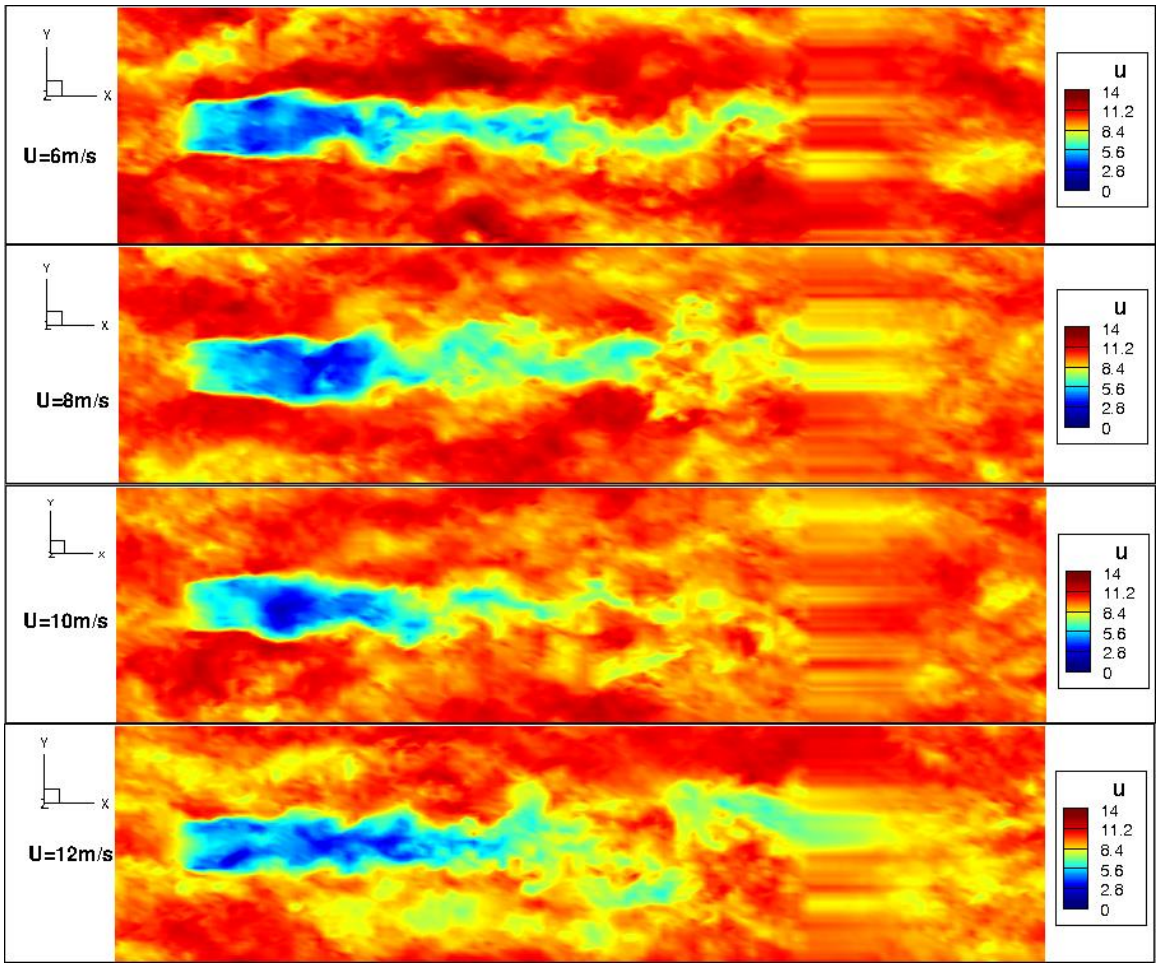

Figure 4.1 Contour plot of the instantaneous velocity of the single wind turbine cases with Ct=1.997 at z=100m.

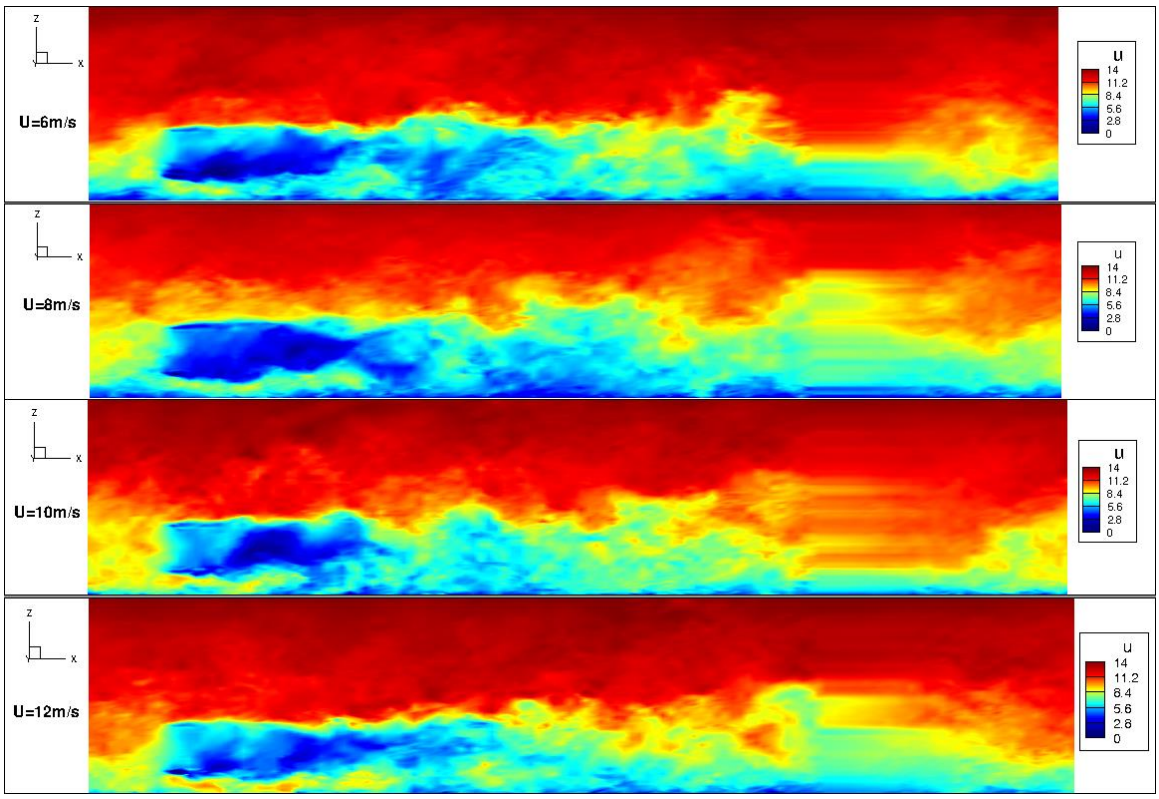

Figure 4.2 Contour plot of the instantaneous velocity of the single wind turbine cases with Ct=1.997 at y=250m.

Figures 4.3-4.7 represent the contour plots of the time-averaged streamwise velocity, humidity and temperature, respectively, in sections through the domain at elevations of z=50m (below the hub), z=100m (through the hub) and z=150m (above the hub). From these figures, we can remark the behavior of wake behind the wind turbine: there is a velocity deficit behind the wind turbine, which persist for long distances in the downstream. There is also a decrease in the humidity below the hub height and an increase above, and the humidity wake seems to split into two branches further in the downstream (about 3-4 diameters); finally, the variation in temperature is very weak.

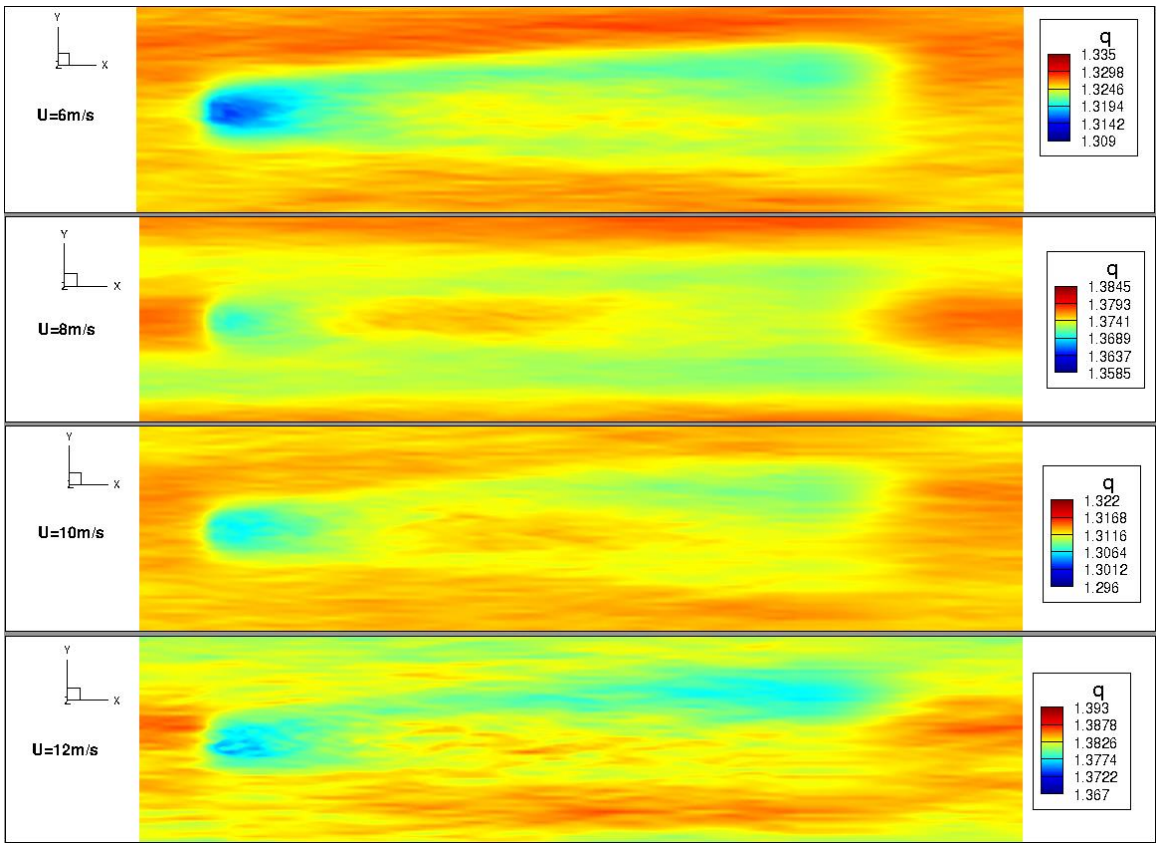

Figure 4.3 Contour plot of the average humidity of the single wind turbine cases with Ct=1.997 at z=50m.

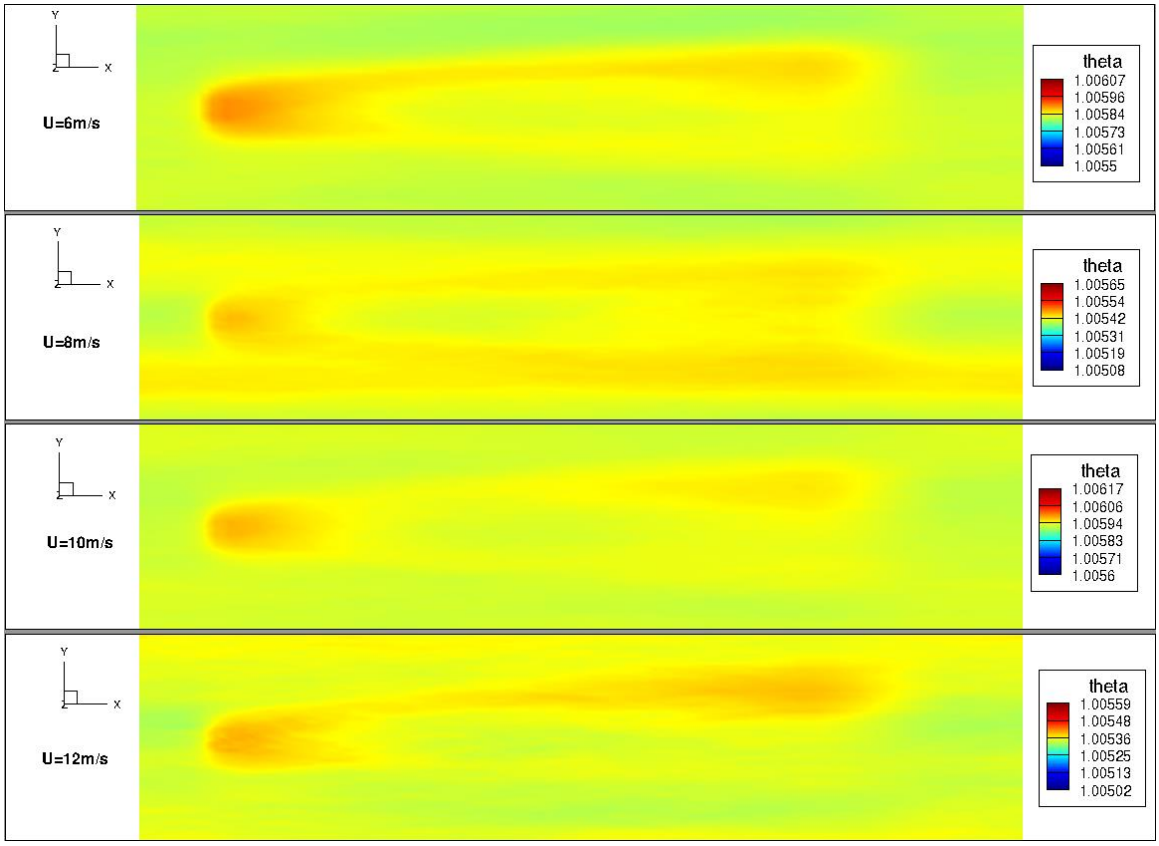

Figure 4.4 Contour plot of the average temperature of the single wind turbine cases with Ct=1.997 at z=50m.

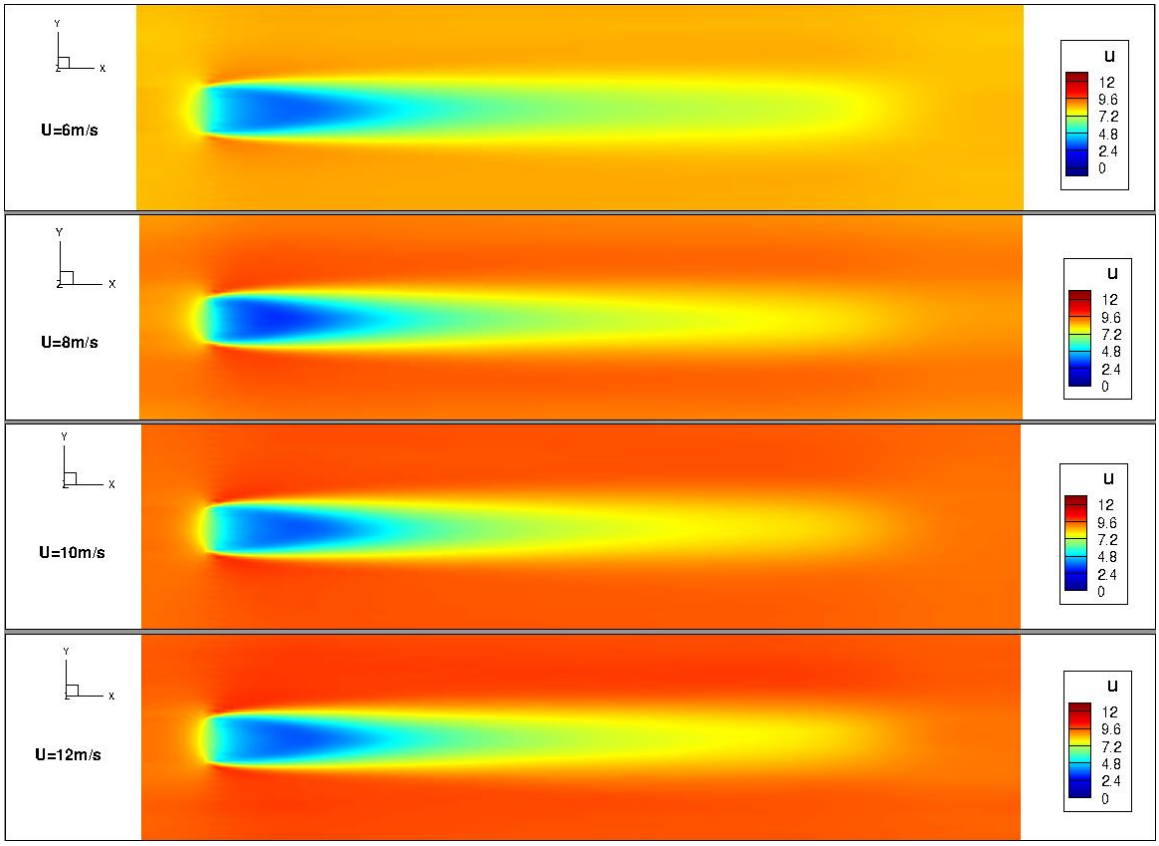

Figure 4.5 Contour plot of the average velocity of the single wind turbine cases with Ct=1.997 at z=100m.

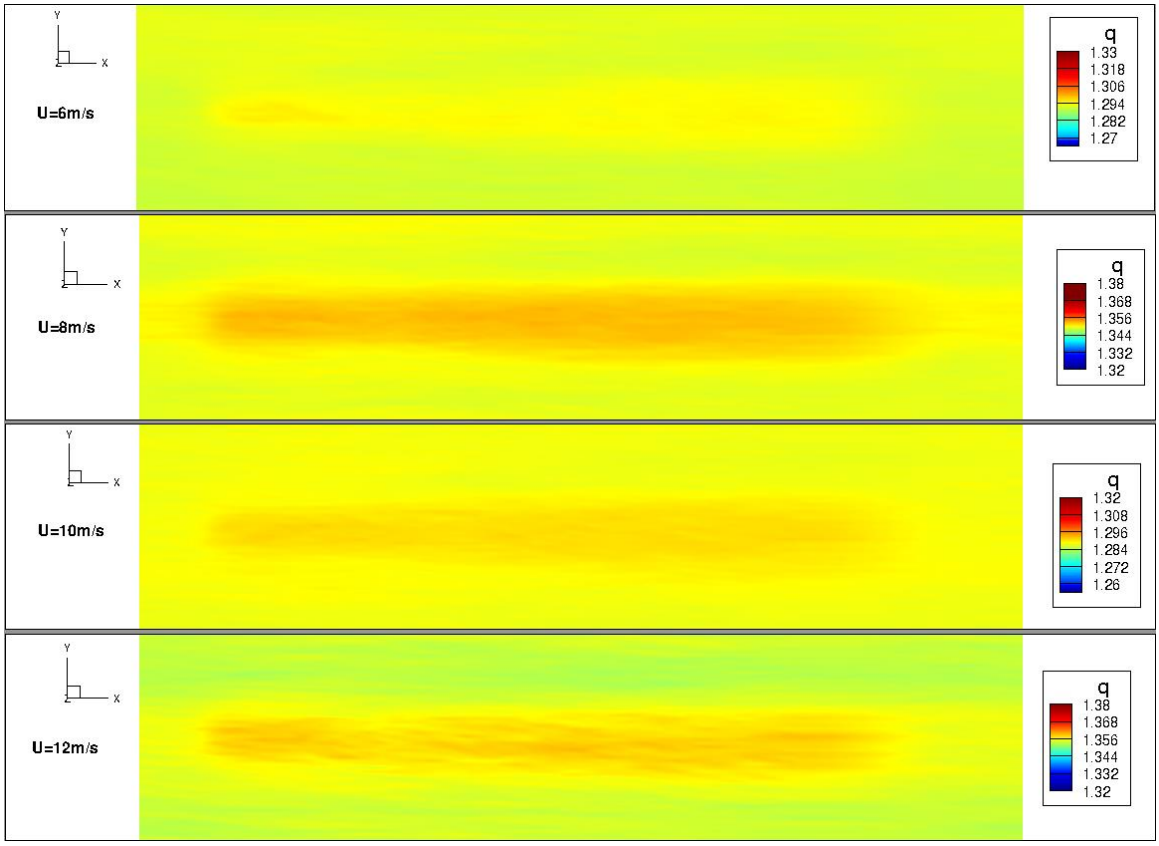

Figure 4.6 Contour plot of the average humidity of the single wind turbine cases with Ct=1.997 at z=150m.

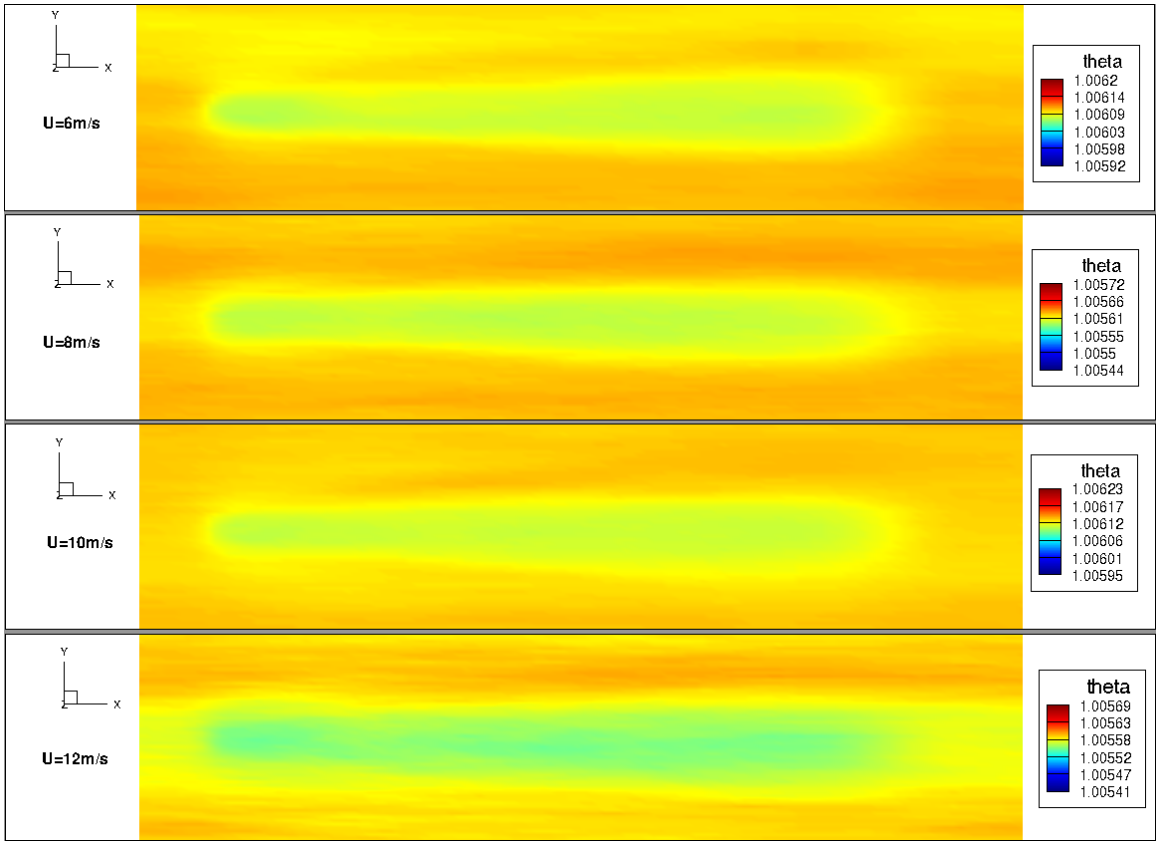

Figure 4.7 Contour plot of the average temperature of the single wind turbine cases with Ct=1.997 at z=150m.

Next, Figure 4.8 shows clearly the wake developing and fading in the downstream of the rotor; the wake is characterized by a velocity deficit and a shear layer that generates turbulence. The dissipation of the wake at the end of the domain is not physical, but the outcome of imposing flow conditions from the precursor simulations using a blending region.

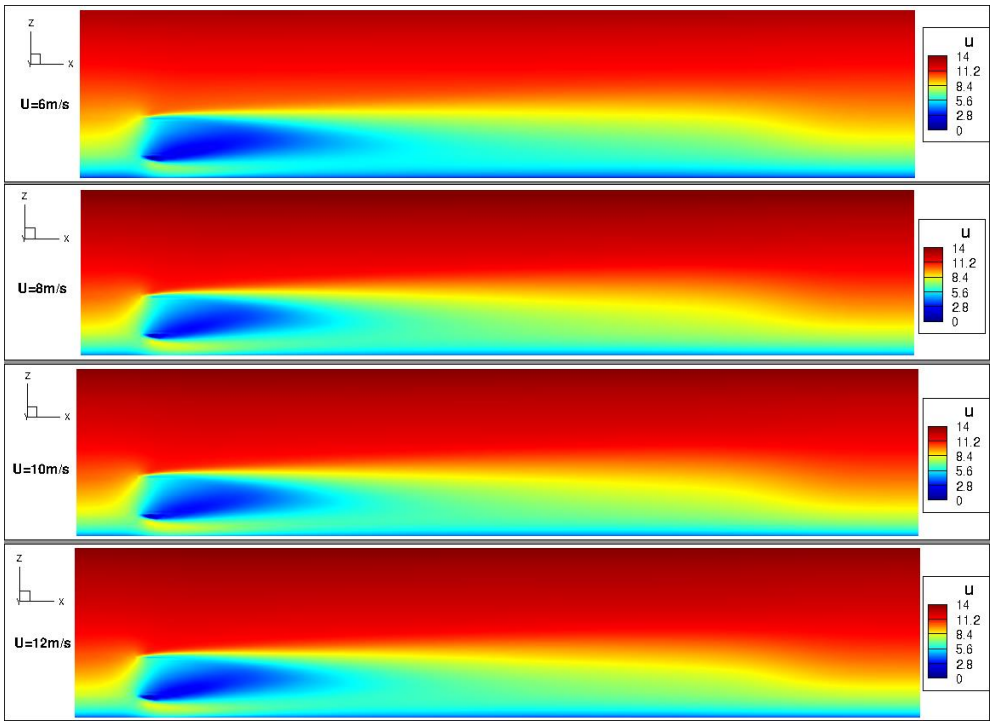

Figure 4.8 Contour plot of the average velocity of the single wind turbine cases with Ct=1.997 at y=250m.

Next, we should discuss the velocity profiles along the vertical (z) direction and lateral (y) direction. Then, we will move the discussion to the temperature profiles along the lateral direction, and finally, we will discuss the humidity profiles along the lateral direction and the variation of the specific humidity along the vertical direction.

In the following cases, the same range has been used between each graph tick values to be able to compare the results among them. This way allowed us to be able to perform comparisons both qualitatively and quantitatively.

Velocity profiles:

The following figures represent profiles of the averaged velocity along the vertical z- and lateral y-directions:

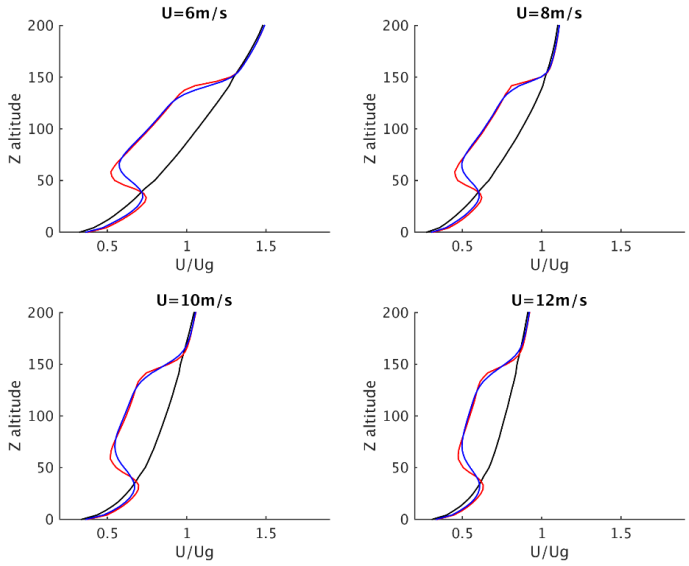

Figure 4.9 Vertical profiles of U/Ug for constant Ct=0.761 for different velocities. In red wake at 1.5D, in blue wake 2.5D and black the front of the wind turbine.

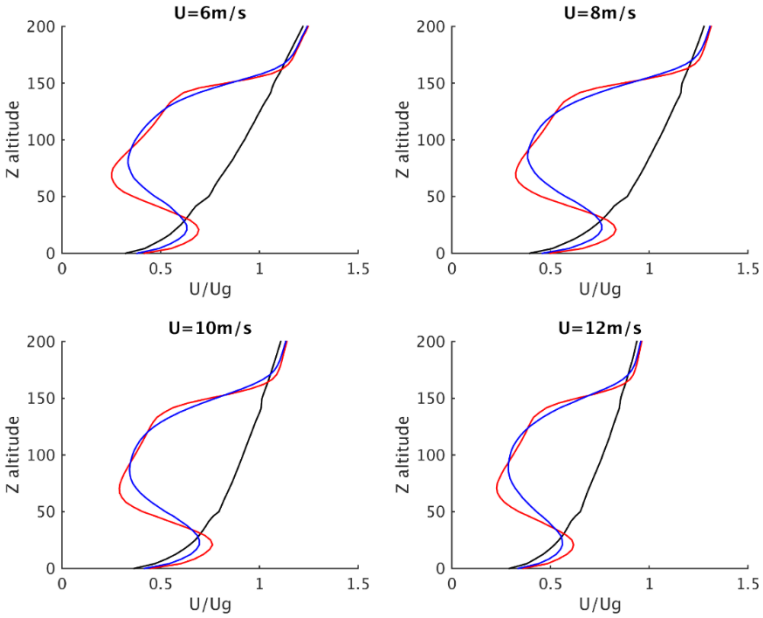

Figure 4.10 Vertical profiles of U/Ug for constant Ct=1.997 for different velocities. In red wake at 1.5D, in blue wake 2.5D and black the front of the wind turbine.

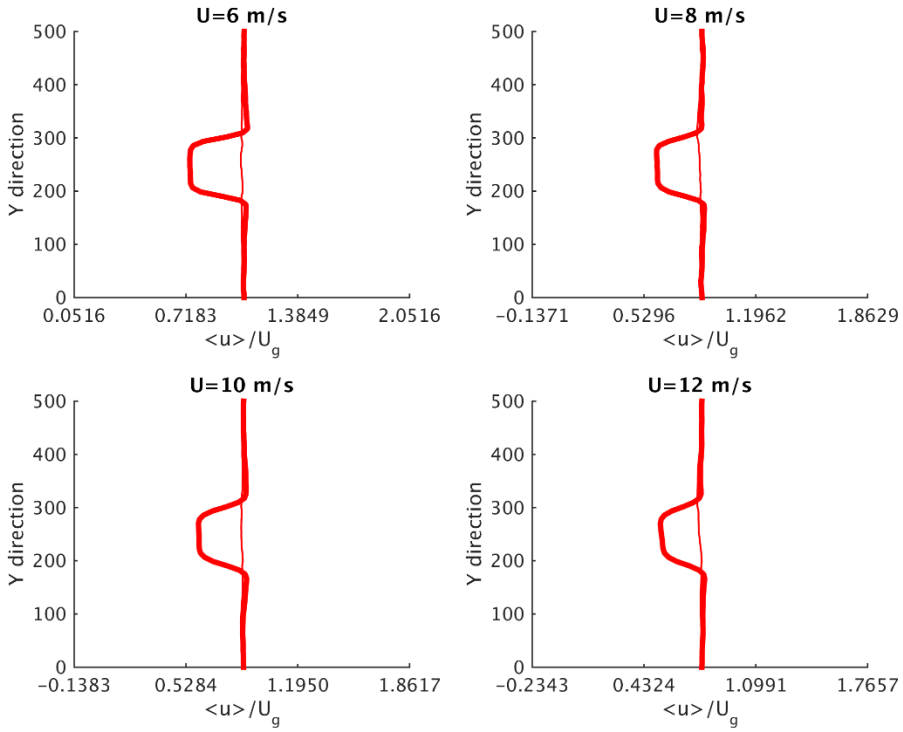

Figure 4.11 Lateral profiles of U/Ug for constant Ct=0.761 for different velocities. Thin line: upstream, bold line: at 1.5D in the wake. In red at hub height 100m.

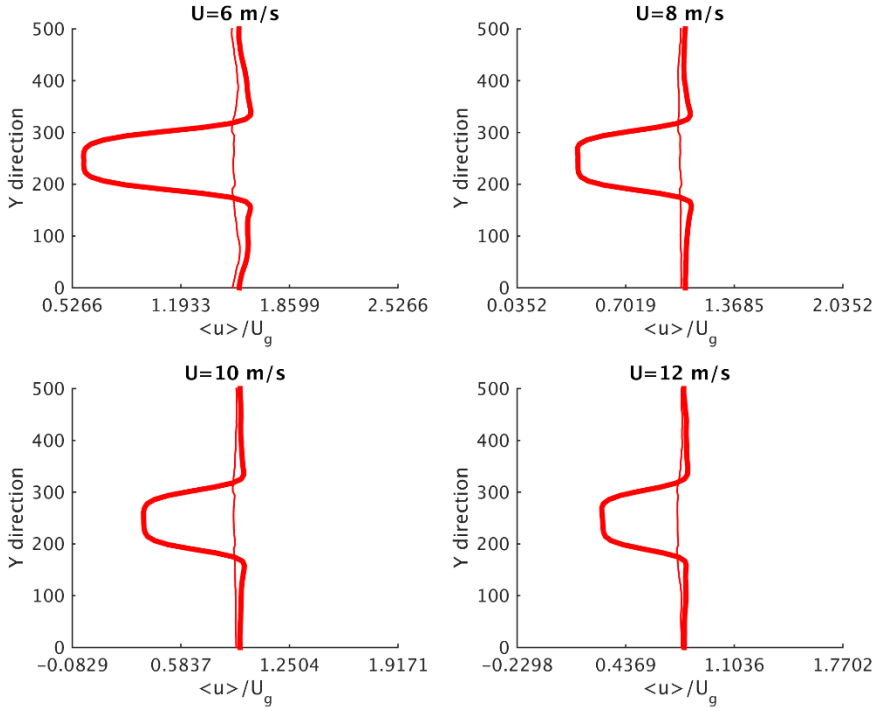

Figure 4.12 Lateral profiles of U/Ug for constant Ct=1.997 for different velocities. Thin line: upstream, bold line: at 1.5D in the wake. In red at hub height 100m.

As the wind turbine blades are spinning, a portion of the momentum and energy from the surrounding flow is transferred to the wake. As the thrust coefficient is increased, a high quantity of momentum and energy is transferred to the blades. This observation can be seen in Figures 4.9 and 4.10 above where the increase of the thrust coefficient shows the decrease of the velocity due to the transfer of the large quantity of kinetic energy. Secondly, as we go down stream, the wake velocity starts to return to the upfront velocity values, and this is due to the wake dissipating into the atmosphere. The shape of the curve is kept the same for all the velocities used, but as we increase the velocity (example case U=10m/s or U=12m/s) we can see that the acceleration below the

hub is reduced. However, this acceleration area is present both above and below the hub, but it is more visible below due to the presence of the solid ground.

In Figures 4.11 and 4.12, time-averaged velocity distribution is plotted along the lateral y-direction at 1.5 diameters from the hub, including the profile upstream of the hub (at one diameter upstream). Along the lateral direction, we will focus mainly on the wake curves (bold line) since the change happens in the wake mostly. One can notice that for higher velocities (U=10m/s and U=12m/s) the velocity in the wake increases. We can see that an increase of the thrust coefficient decreases considerably the velocity in the y direction. Along the lateral direction, we can notice the area of acceleration across the wind turbine. The velocity of the flow decreases from case to case at the hub height due to the extraction of momentum from the surrounding flow. These observations are complementary with the ones found in the profiles along the vertical direction (z altitude).

4.3 Temperature profiles:

The following figures represent the temperature profiles along the lateral direction:

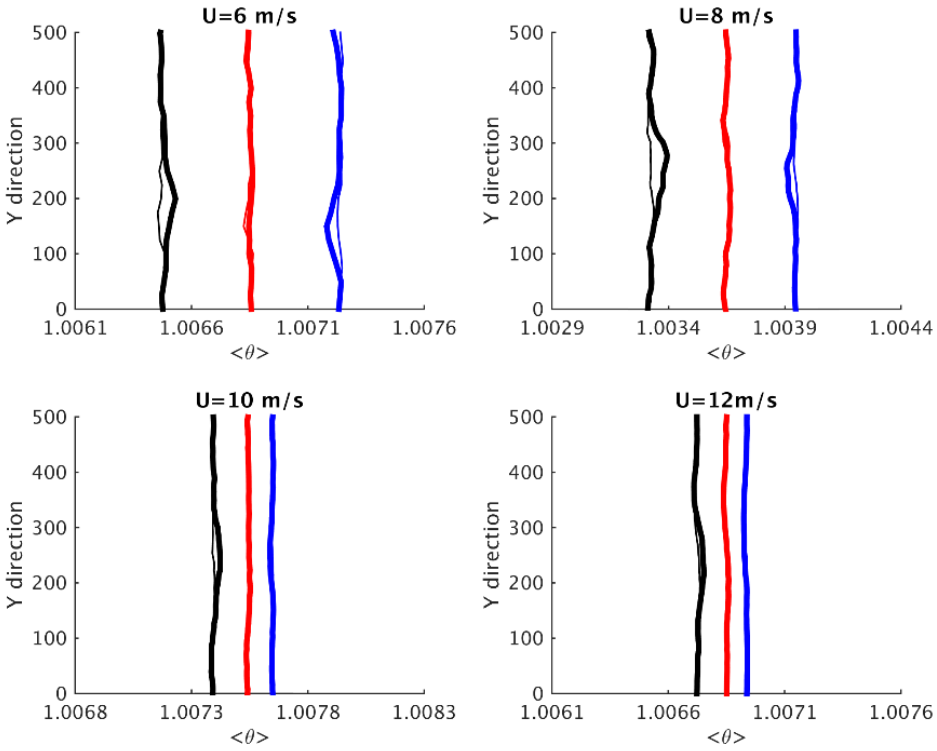

Figure 4.13 Lateral profiles of the temperature for constant Ct=0.761 for different velocities.

Thin line: upstream, bold line: wake at 1.5D. In red at hub height z=100m, in blue above the hub height z=150m and black below the hub height z=50m.

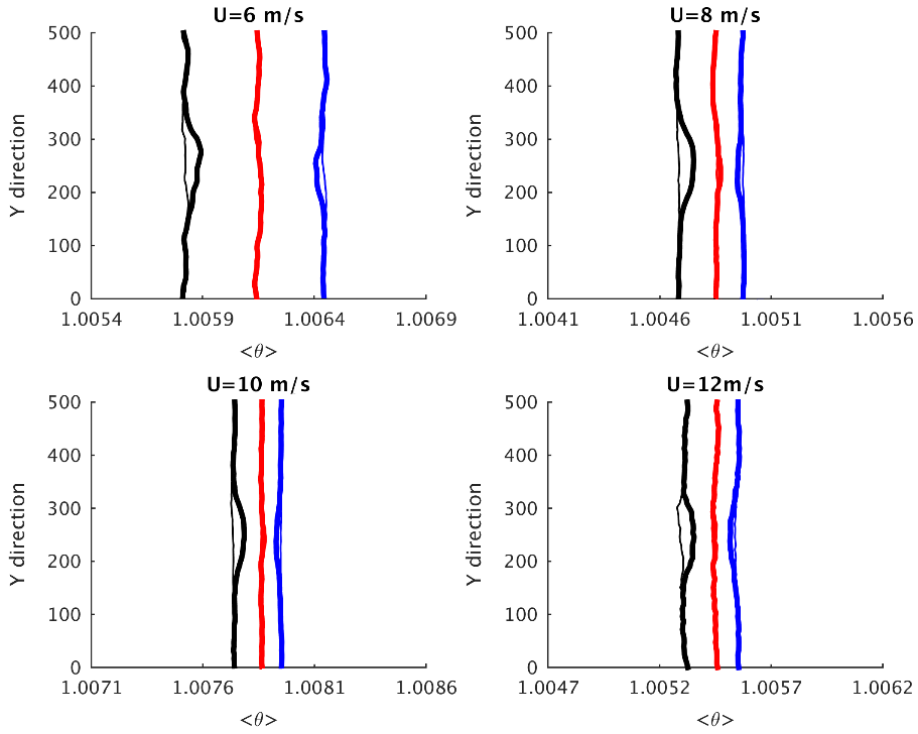

Figure 4.14 Lateral profiles of temperature for constant Ct=1.997 for different velocities.

Thin line: upstream, bold line: wake at 1.5D. In red at hub height z=100m, in blue above the hub height z=150m and black below the hub height z=50m.

As shown in Figures 4.13 and 4.14, a variation of the temperature is mainly present below the hub and above it, and this change in the potential temperature is very small between downstream and upstream. We can also add that the potential temperature below the hub decreases in the wake. These almost steady curves can be explained by the stratification being a constant. The velocity of a cool fluid is higher than a hot fluid, a high level of mixing occurs with the increase in the velocity. By increasing of the thrust coefficient, the variation of temperature between the wake and the upstream value is higher.

4.4 Humidity profiles:

The following profiles represent the specific humidity along the y- and z-direction, where the percentage of the specific humidity change for the vertical direction is reported.

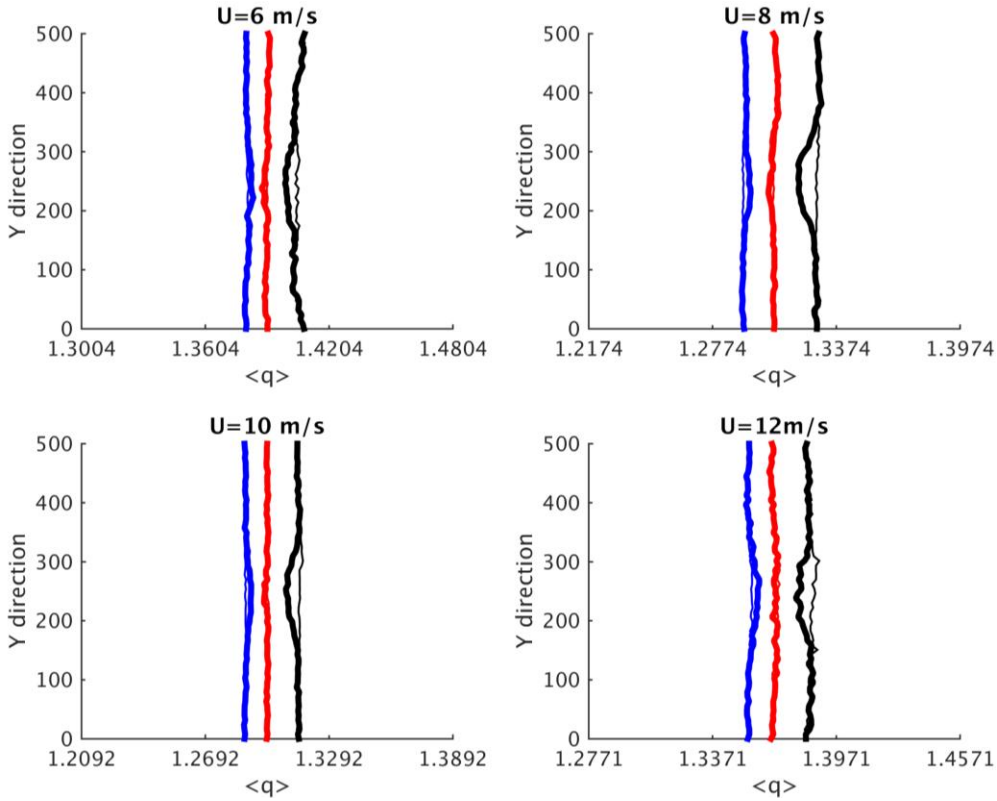

Figure 4.15 Lateral profiles of humidity for constant Ct=0.761 for different velocities.

Thin line: upstream, bold line: wake at 1.5D. In red at hub height z=100m, in blue above the hub height z=150m and black below the hub height z=50m.

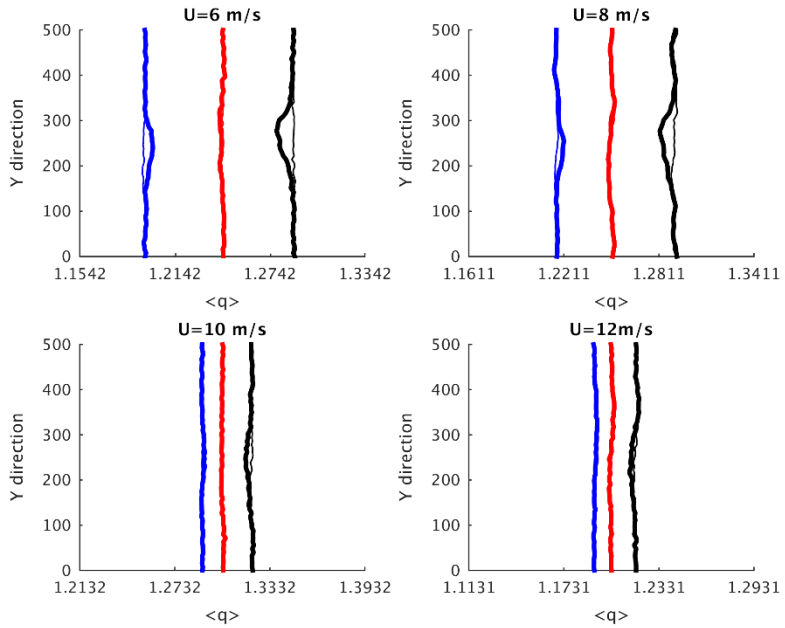

Figure 4.16 Lateral profiles of humidity direction for constant Ct=1.997 for different velocities.

Thin line: upstream, bold line: wake at 1.5D. In red at hub height z=100m, in blue above the hub height z=150m and black below the hub height z=50m.

From the previous figures, the variation of the humidity along the lateral direction is calculated, and the values are listed in the next table.

Table 4.3 Variation of the specific humidity for all single wind turbine cases.

CASES SINGLE WIND TURBINE	VARIATION OF SPECIFIC HUMIDITY %	
	BELOW	ABOVE
ST1	-1.43 %	+0.85%
ST2	-1.33%	+0.50%
ST3	-0.37%	+0.11%
ST4	-0.28%	+0.19%
ST5	-0.81%	+0.405%
ST6	-0.749%	+0.308%
ST7	-0.57%	+0.271%
ST8	-0.48%	+0.253%

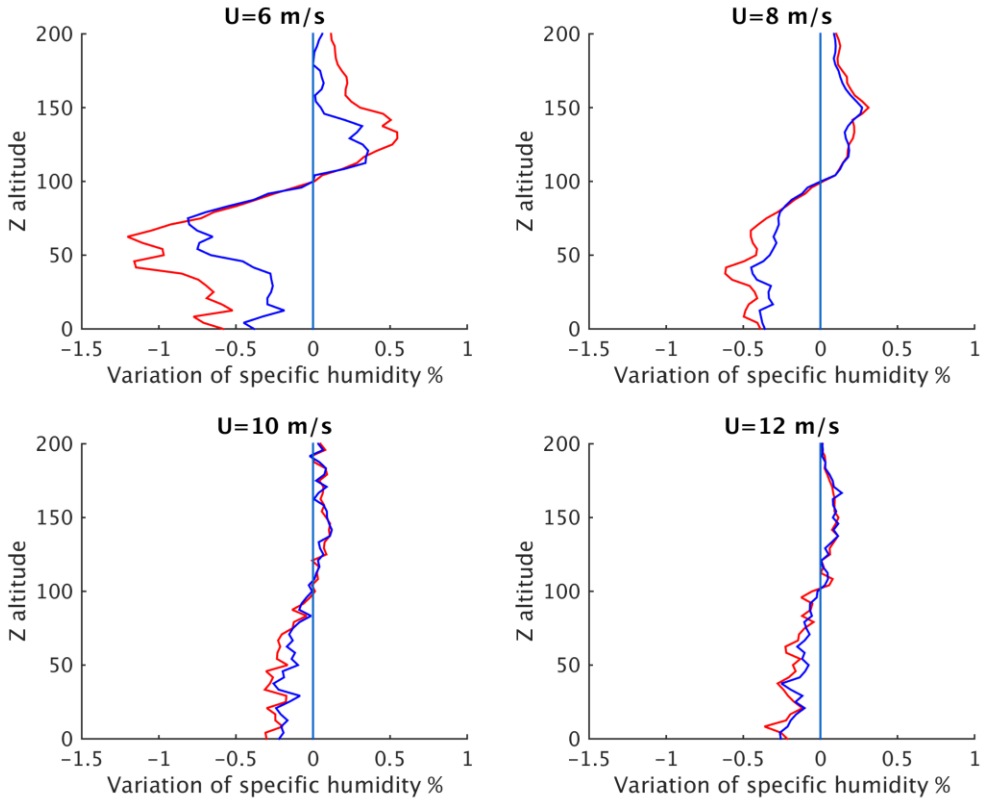

Figure 4.17 Vertical profiles of the variation of the specific humidity for constant Ct=0.761 for different velocities.

In red: wake at 1.5D and blue: wake at 2.5D.

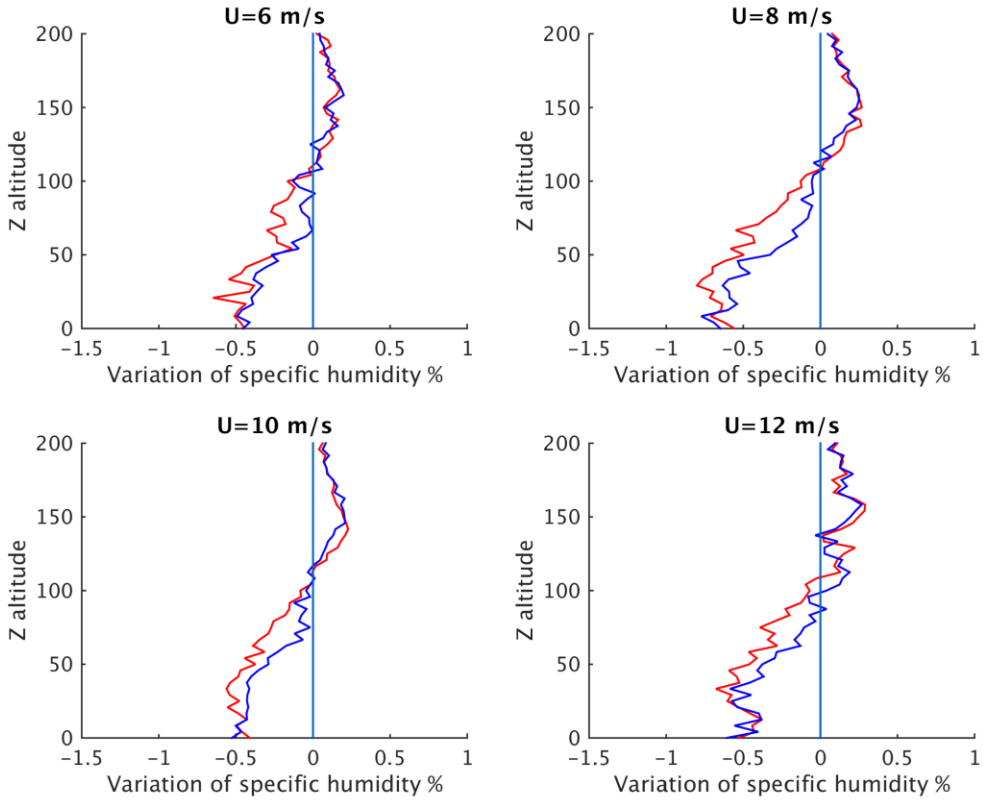

Figure 4.18 Vertical profiles of the variation of the specific humidity for constant Ct=1.997 for different velocities. In red: wake at 1.5D and blue: wake at 2.5D.

For the humidity profiles plotted in Figures 4.17 and 4.18, we can remark that the effect of the wind turbine wake on the humidity is almost the same in both streamwise locations (the largest humidity change was found to occur at 1.5 diameters from the hub). Below the hub height, the variation is felt more than above because of the ground effect.

As we compare the variation of the specific humidity according to the different velocities, we can see that for velocities of 10 m/s and above there is a smaller variation in the specific humidity close to the ground, which can be explained if we go back to the definition of the specific humidity; as the velocity increases, the temperature decreases;

therefore, colder air cannot hold more water. The same pattern can be seen above the hub at 150m from the ground: higher velocities provide low variation of the specific humidity. The thrust coefficient affects principally the wind velocity which only confirms the pattern for the variation of the specific humidity. The wind turbine acts as an inflection point that modifies the behavior between the above and below the hub.

4.5 Wind farm

After discussing the case of a single turbine in the previous section, we will move to the case of a wind farm (4x4). The domain extents in the streamwise, span wise and vertical direction are: 2000π m, 500π m and 400 m. The first wind turbine of the first row is located at x=600m and y=180m with respect to the inflow boundary and the lateral boundary, respectively. Two values of thrust coefficient associated with the wind turbine rotors (1.997 and 0.333) and three values of the wind velocity (6, 8 and 10 m/s) are considered.

The three following contour plots figures show contour plots of the instantaneous and average streamwise velocity, specific humidity and potential temperature in sections through the domain at z=50m (below the hub), z=100m (through the hub) and z=150m (above the hub).

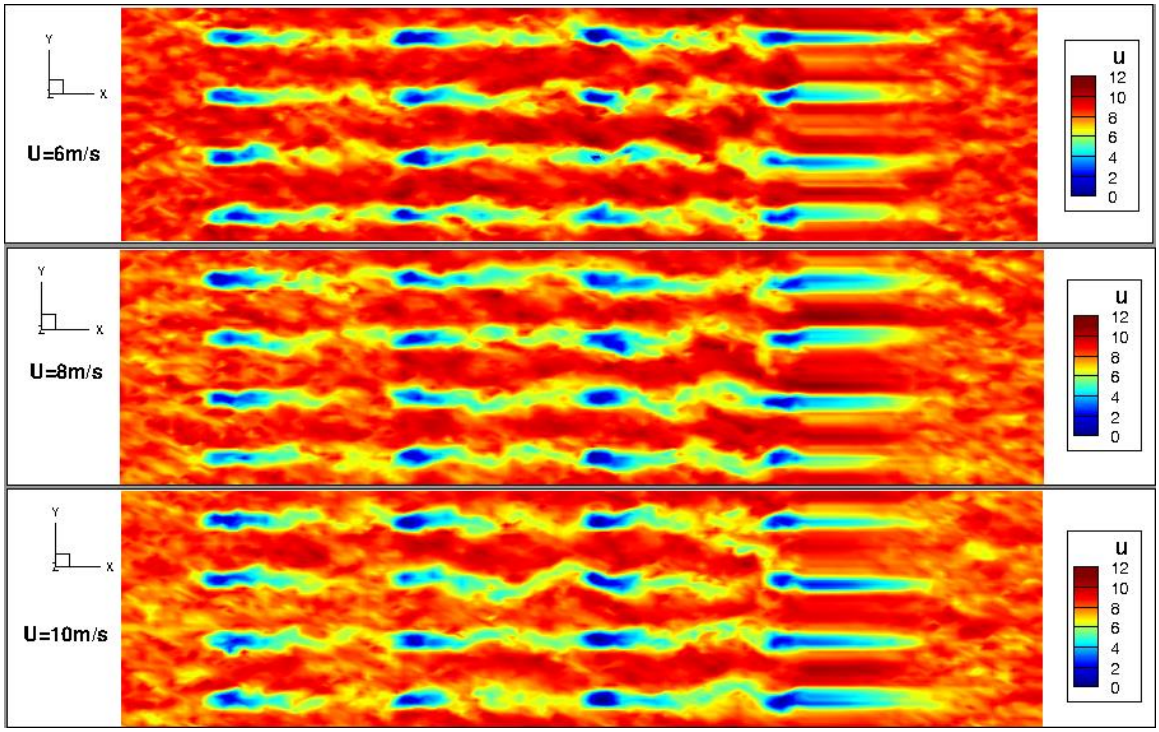

Figure 4.19 Contour plot of the instantaneous velocity of the wind farm cases with Ct=1.997 at z=100m.

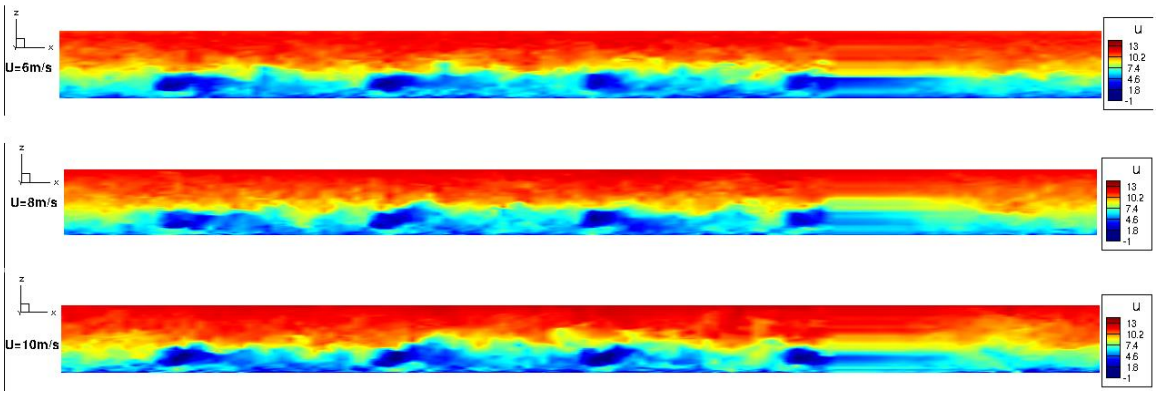

Figure 4.20 Contour plot of the instantaneous velocity of the wind farm cases with Ct=1.997 at y=180m.

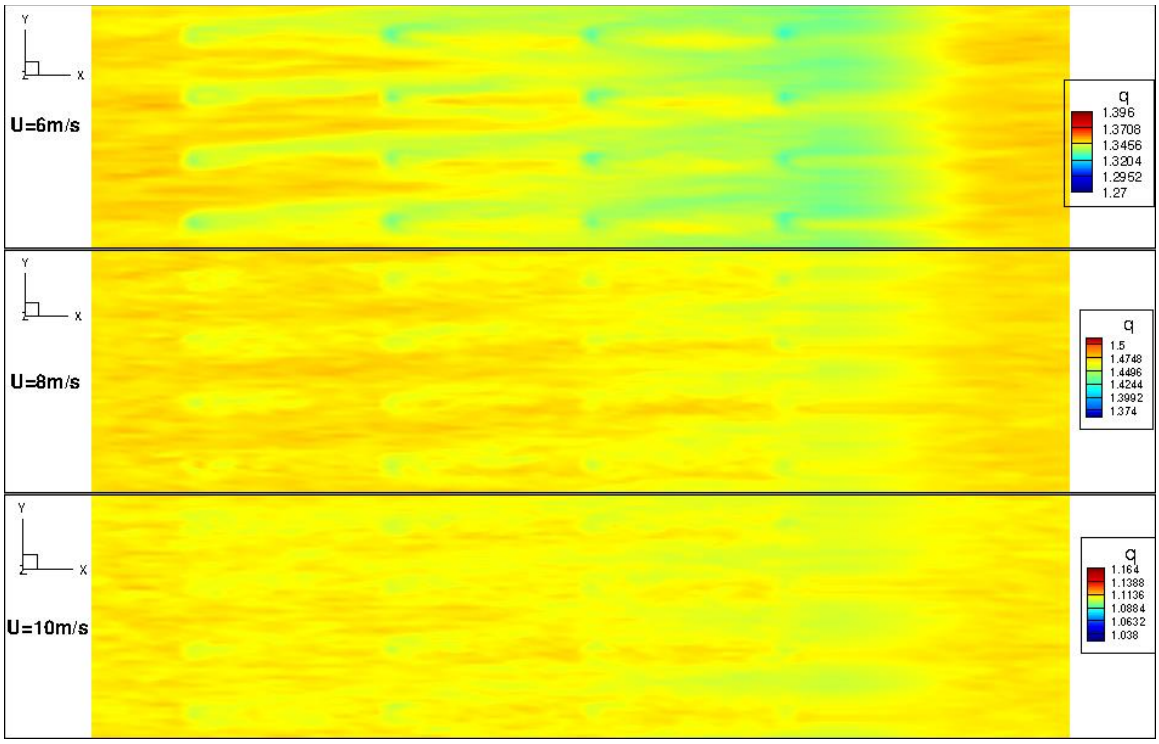

Figure 4.21 Contour plot of the average humidity of the wind farm cases with Ct=1.997 at z=50m.

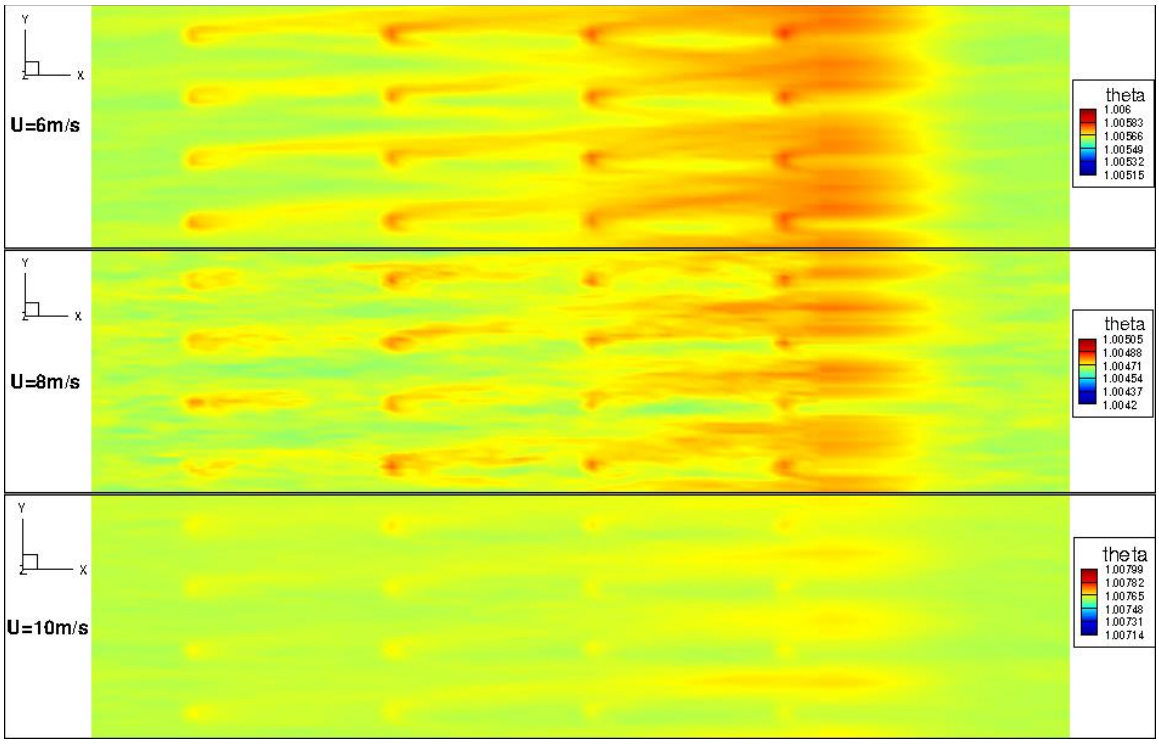

Figure 4.22 Contour plot of the average temperature of the wind farm cases with Ct=1.997 at z=50m.

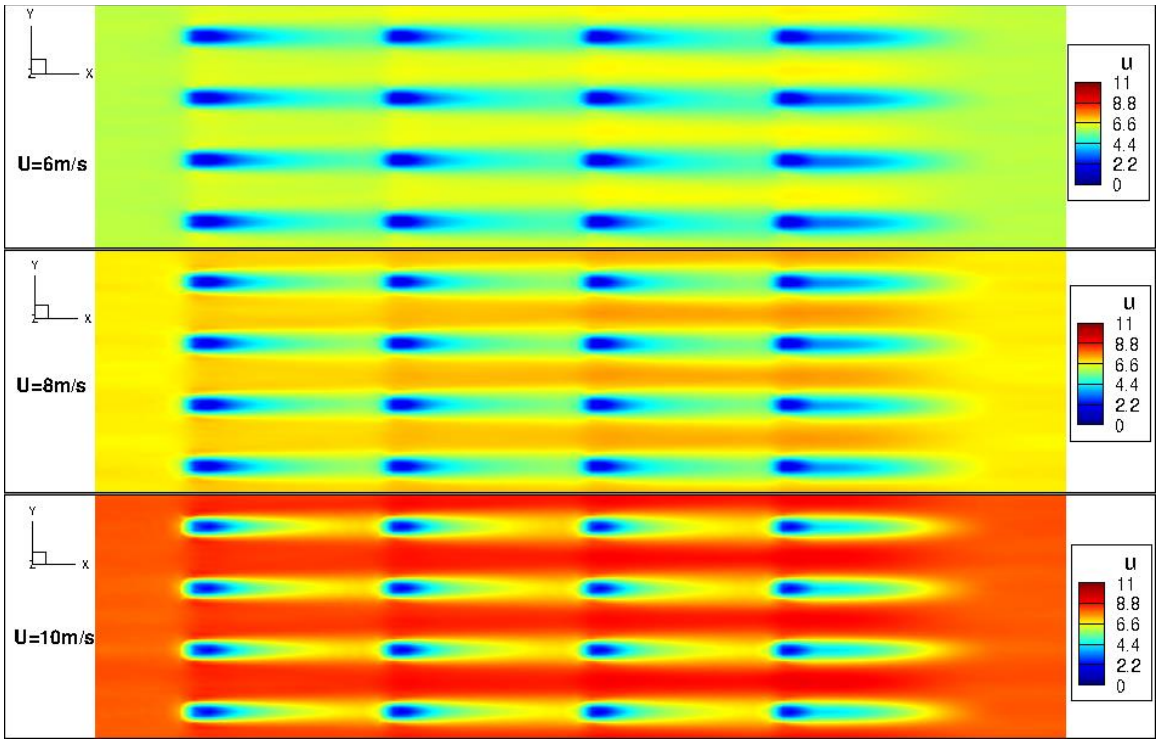

Figure 4.23 Contour plot of the average velocity of the wind farm cases with Ct=1.997 at z=100m.

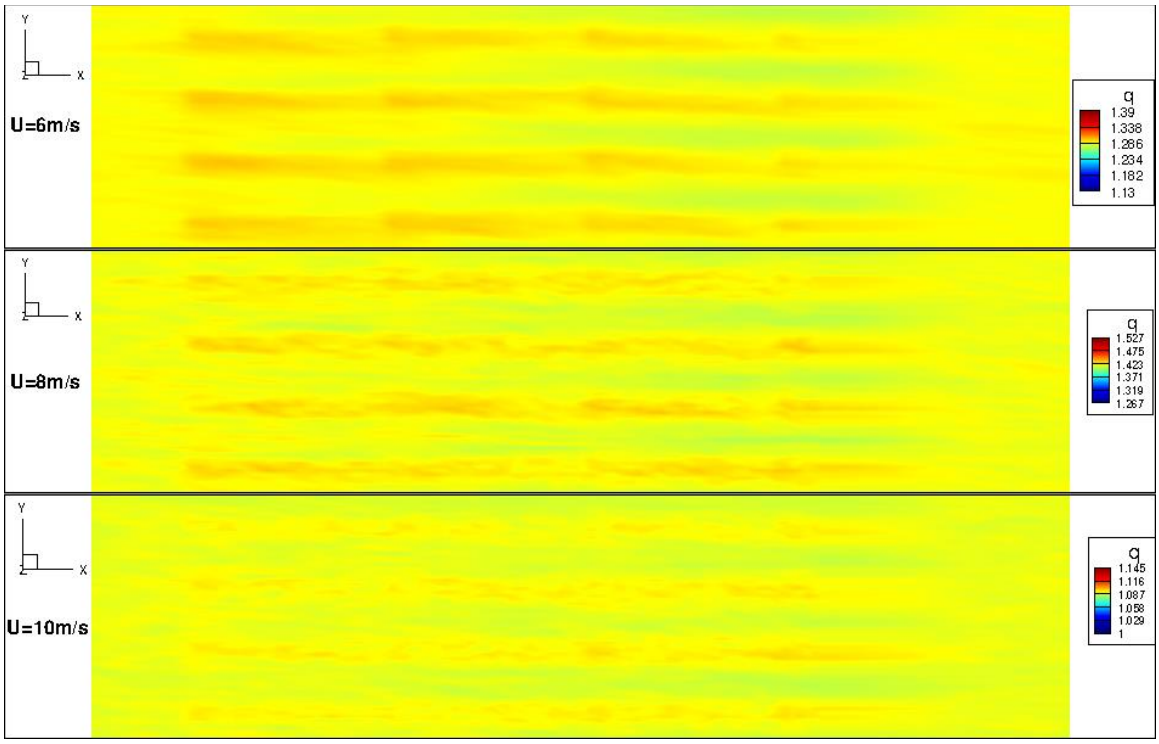

Figure 4.24 Contour plot of the average humidity of the wind farm cases with Ct=1.997 at z=150m.

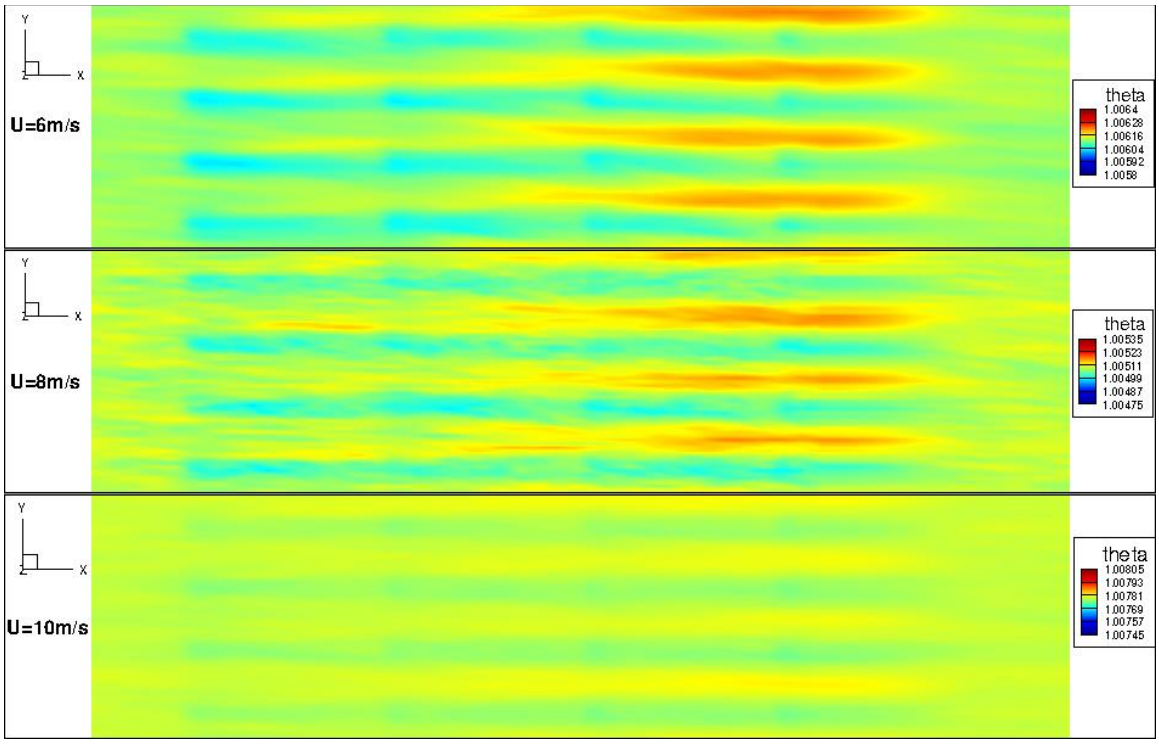

Figure 4.25 Contour plot of the average temperature of the wind farm cases with Ct=1.997 at z=150m.

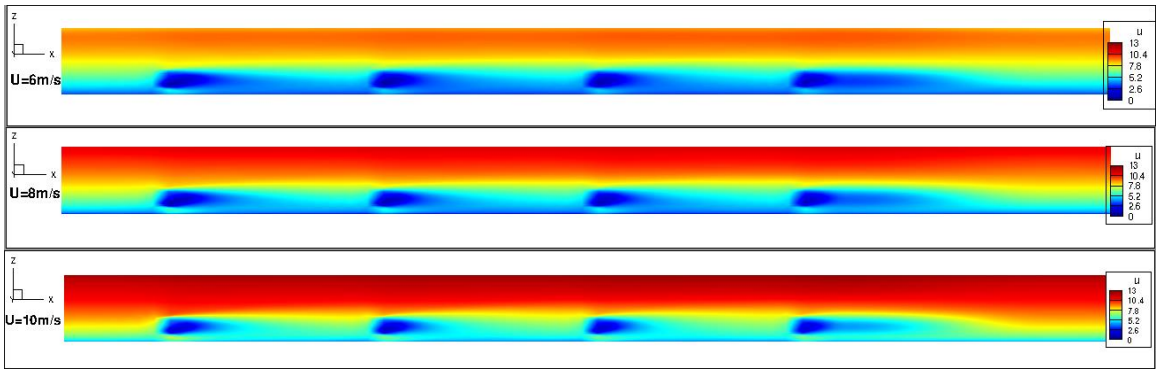

Figure 4.26 Contour plot of the average velocity of the wind farm cases with Ct=1.997 at y=180m.

In the instantaneous contour plots of the velocity shown in Figures 4.19 and 4.20, one can notice the turbulence wakes shedding from the wind turbines and how each wake interacts with the wake generated by the upstream wind turbine. We can remark from the

set of contour plots following the instantaneous snapshots the deficit of the flow velocity in the wake, and how it can affect the next wind turbine located upstream in the same direction. We can also notice the wakes shedding from the wind turbines and how the wake of first turbines is transferred into the following one located downstream, which can have an accumulating effect. From these contours - especially the velocity contour plot along the y direction - we can observe that the flow behind the wind turbine disk is pinched back in front of the next wind turbine. Below the wind turbine around 50m from the ground, we can remark clearly the flow being pushed back in front of the next wind turbine due to the proximity to the solid ground. Above the wind turbine around 150m, it is not as visible because the flow can go to the upper atmosphere and experience mixing.

4.6 Velocity profiles:

The following figures represent the velocity along the vertical and lateral direction:

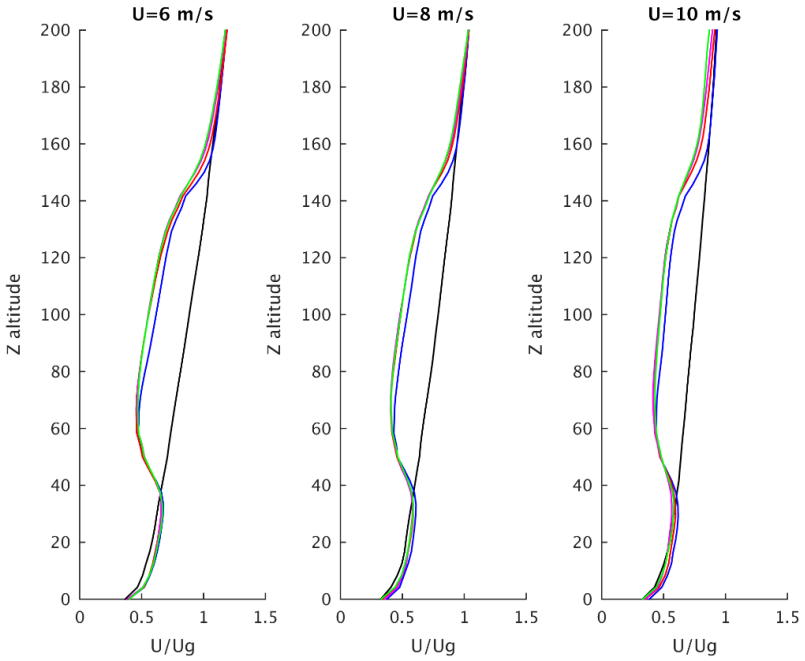

Figure 4.27 Vertical profile of the average velocity along z for Ct=0.761 with different velocities.

Black: upstream, blue: wake 1st turbine, red: wake 2nd turbine, magenta: wake 3rd turbine, green: wake 4th turbine.

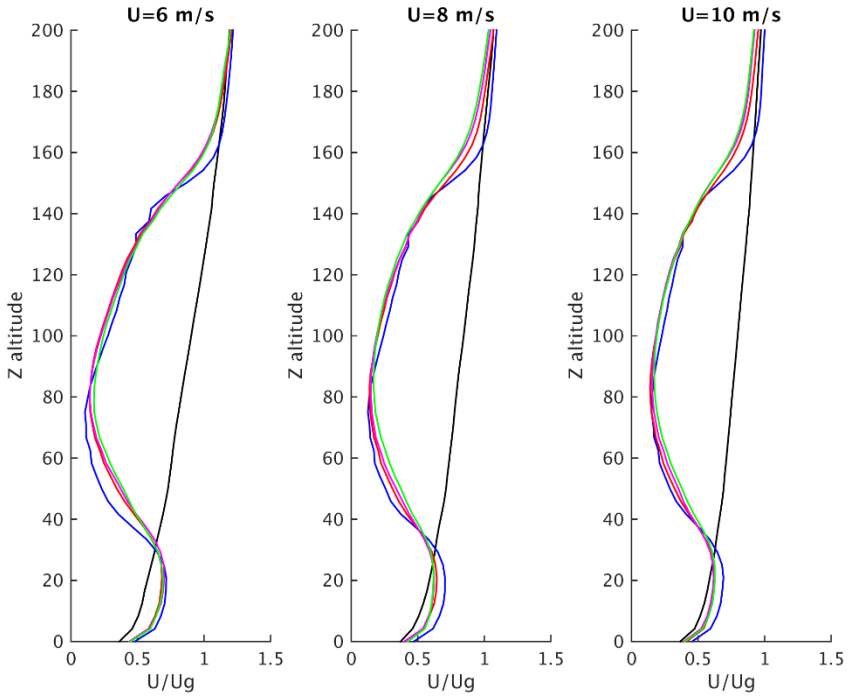

Figure 4.28 Vertical profiles of U/Ug for Ct=1.997 with different velocities.

Black: upstream, blue: wake 1st turbine, red: wake 2nd turbine, magenta: wake 3rd turbine, green: wake 4th turbine.

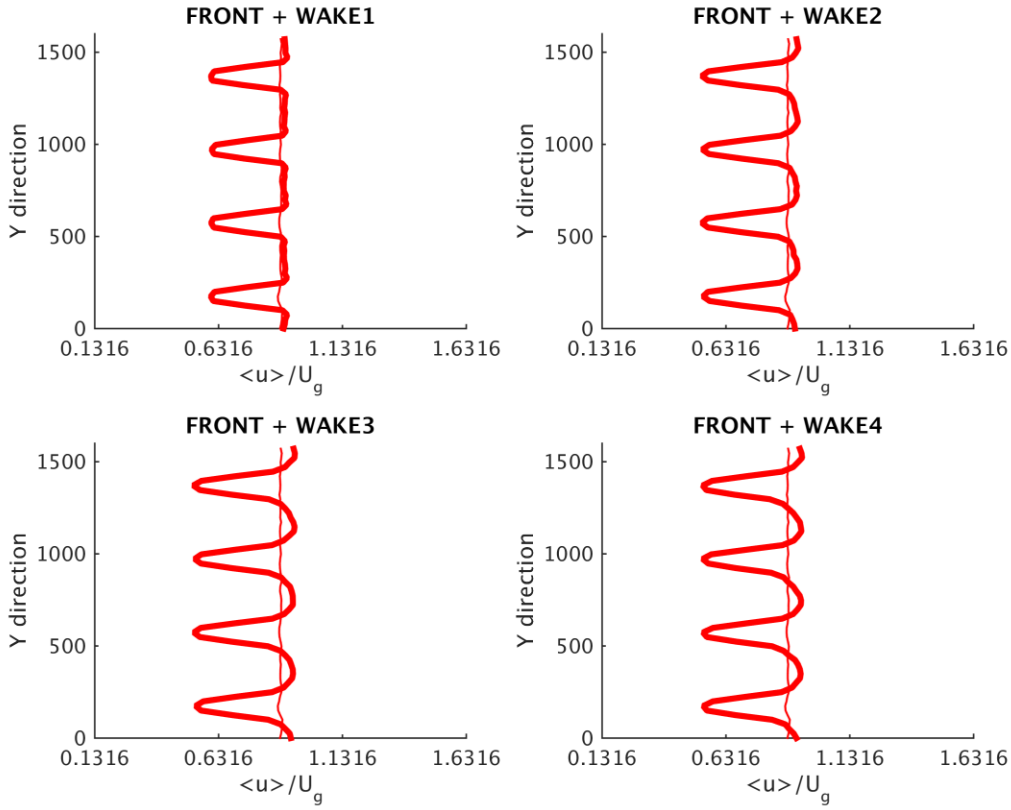

Figure 4.29 Lateral profiles of U/Ug for Ct=0.761 for U=6m/s.

Thin line: upstream, bold line: wake at 1.5D. In red at hub height z=100m.

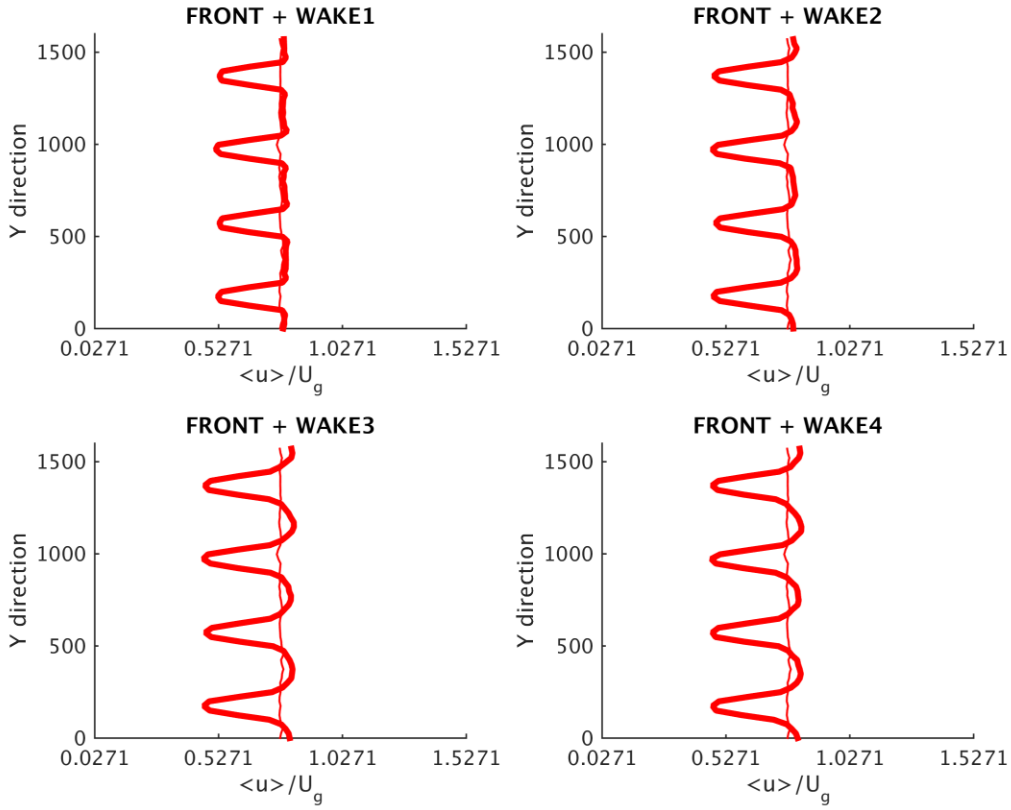

Figure 4.30 Lateral profiles of U/Ug for Ct=0.761 for U=8m/s.

Thin line: upstream, bold line: wake at 1.5D. In red at hub height z=100m.

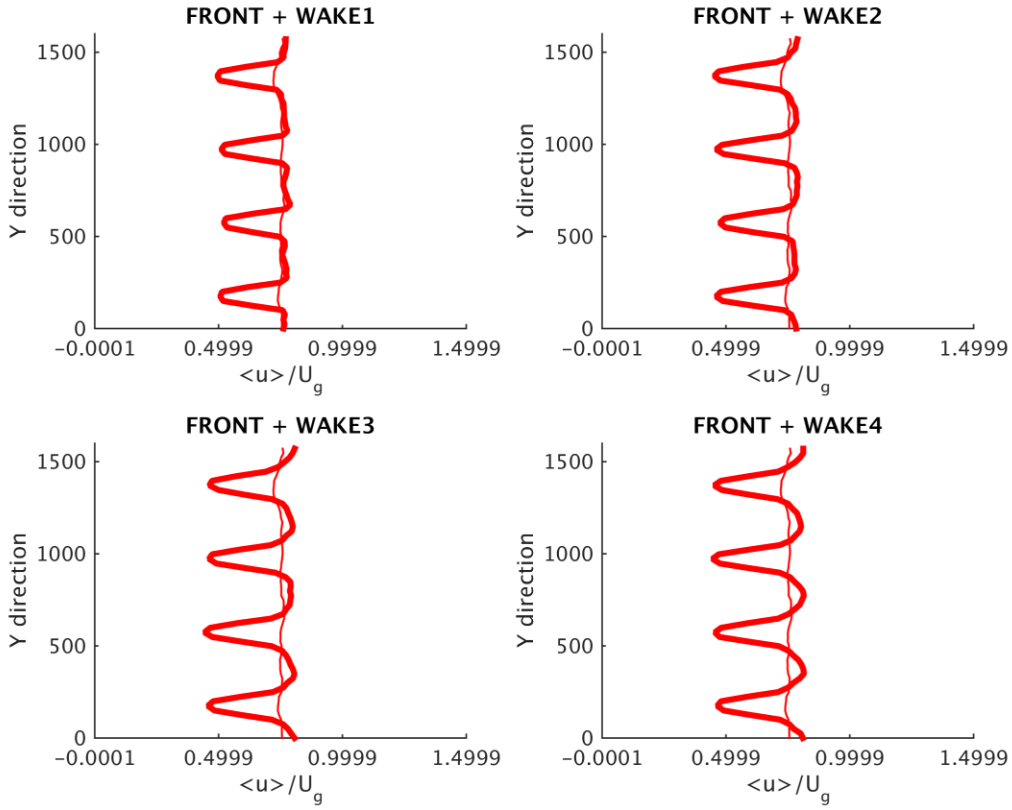

Figure 4.31 Lateral profiles of U/Ug for Ct=0.761 for U=10m/s.

Thin line: upstream, bold line: wake at 1.5D. In red at hub height z=100m.

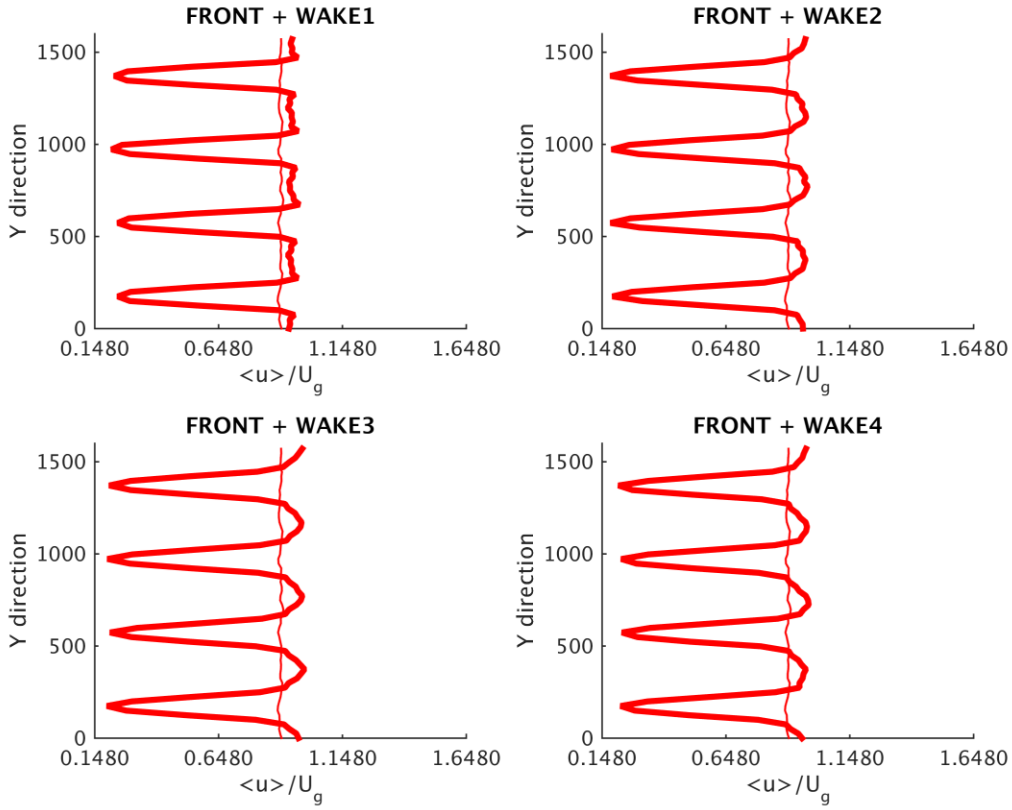

Figure 4.32 Lateral profiles of U/Ug for Ct=1.997 for U=6m/s.

Thin line: upstream, bold line: wake at 1.5D In red at hub height z=100m.

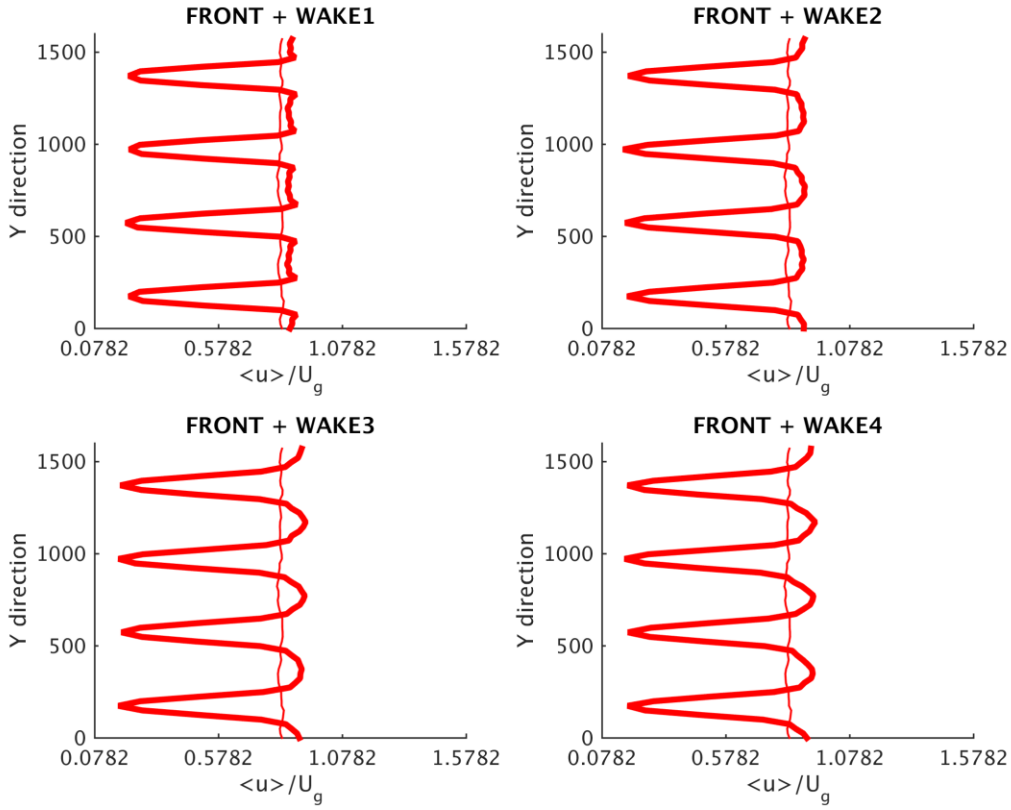

Figure 4.33 Lateral profiles of U/Ug for Ct=1.997 for U=8m/s.

Thin line: upstream, bold line: wake at 1.5D. In red at hub height z=100m.

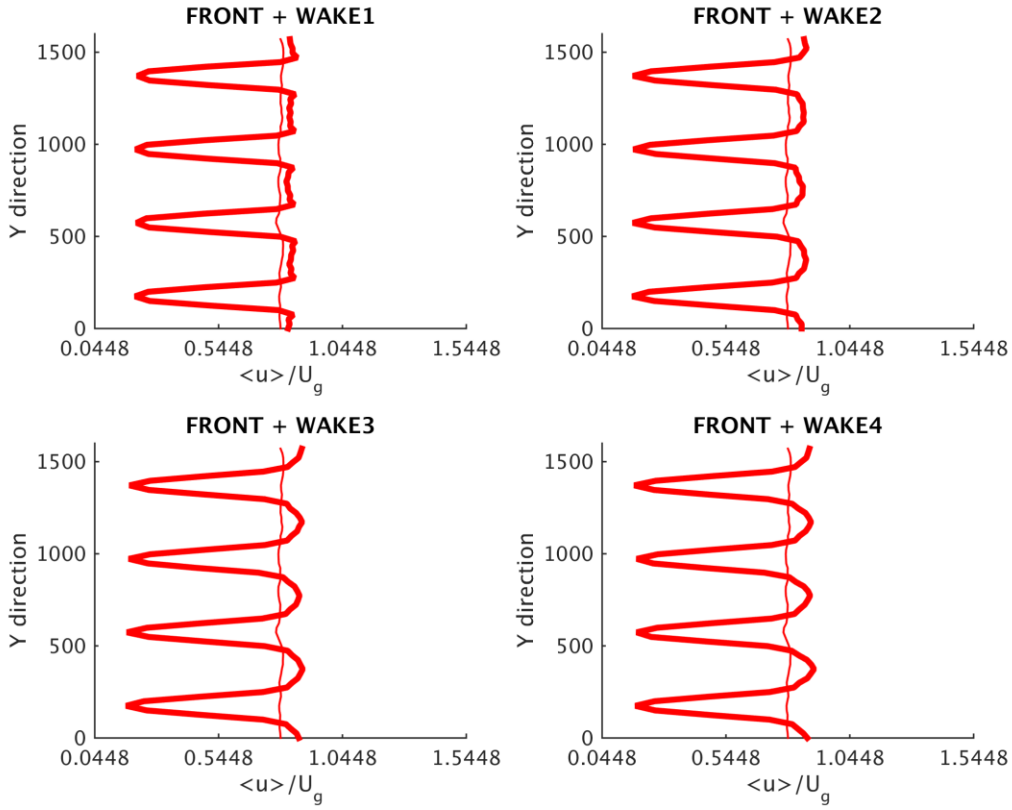

Figure 4.34 Lateral profiles of U/Ug for Ct=1.997 for U=10m/s.

Thin line: upstream, bold line: wake at 1.5D. In red at hub height z=100m.

The velocity profiles along the vertical and lateral direction show how the wakes, different velocities and different thrust coefficients modify the behavior of the flow. From Figures 4.27 and 4.28, we can see that for U=6m/s the wake is spreading more than the two other velocities as the shape of the curve is taller (especially for Ct=1.997). As discussed in the single wind turbine section, the acceleration below the hub is clearly visible with the highest thrust coefficient. We can remark from the figures of the profiles along the lateral direction that at hub height there is a significant deceleration of velocity in the wakes of the turbines. We can also notice from the lateral profiles, a region of

acceleration between wind turbines that increases as we go downstream and as we increase the velocity.

4.7 Temperature profiles:

The following figures represent the potential temperature along the lateral direction:

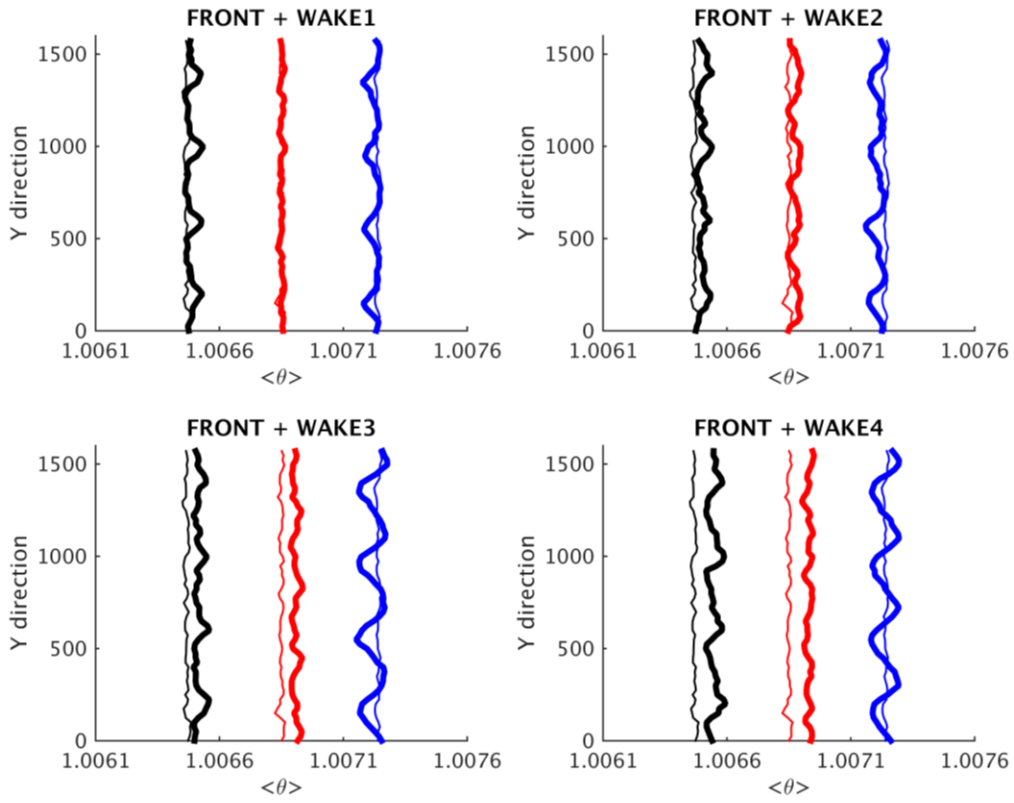

Figure 4.35 Lateral profiles of the temperature for Ct=0.671 for U=6m/s.

Thin line: upstream, bold line: wake at 1.5D. In red at hub height z=100m, in blue above the hub height z=150m and black below the hub height z=50m.

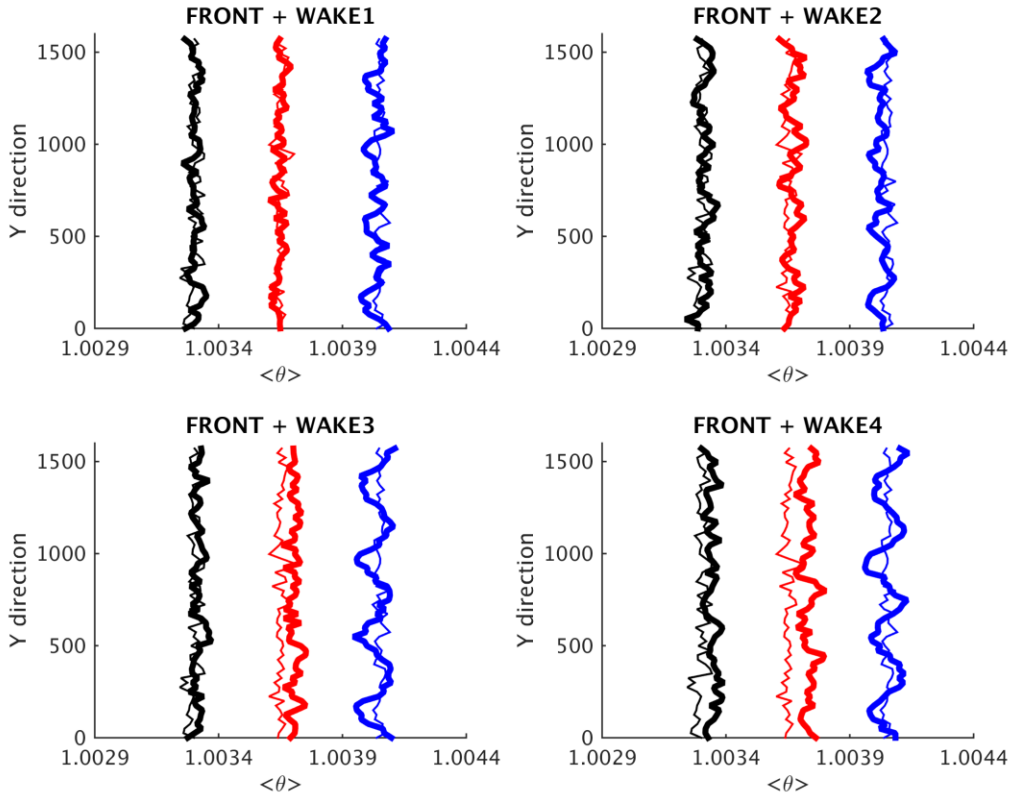

Figure 4.36 Lateral profiles of the temperature for Ct=0.671 for U=8m/s.

Thin line: upstream, bold line: wake at 1.5D. In red at hub height z=100m, in blue above the hub height z=150m and black below the hub height z=50m.

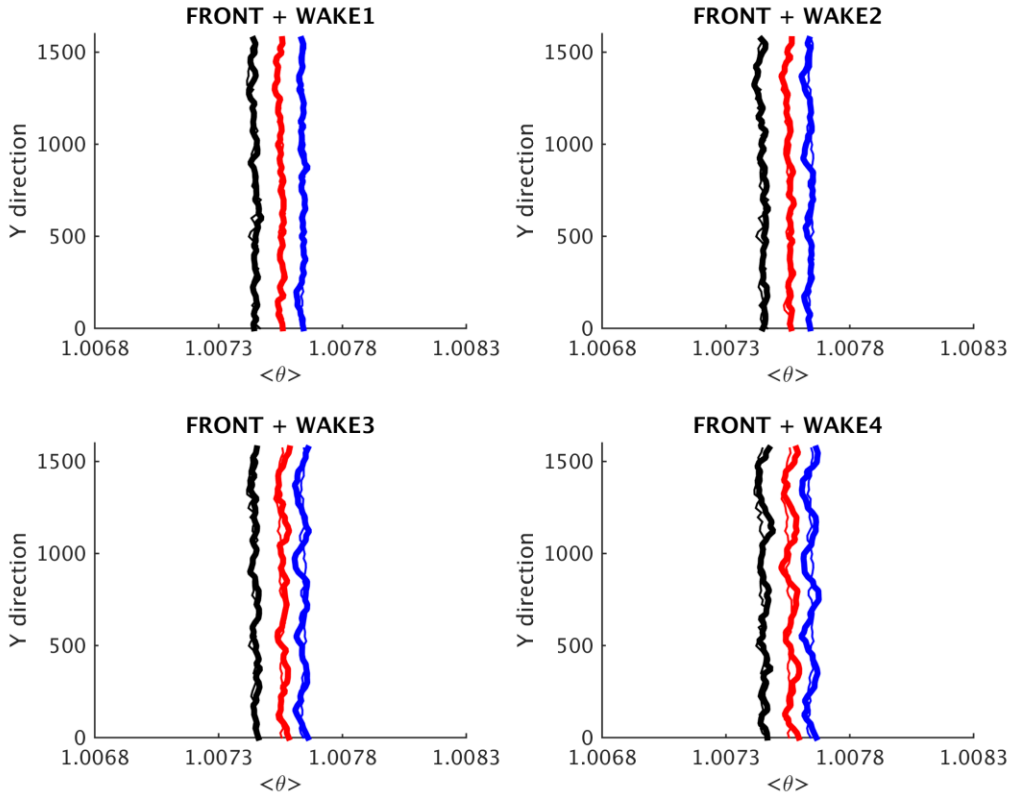

Figure 4.37 Lateral profiles of the temperature for Ct=0.671 for U=10m/s.

Thin line: upstream, bold line: wake at 1.5D. In red at hub height z=100m, in blue above the hub height z=150m and black below the hub height z=50m.

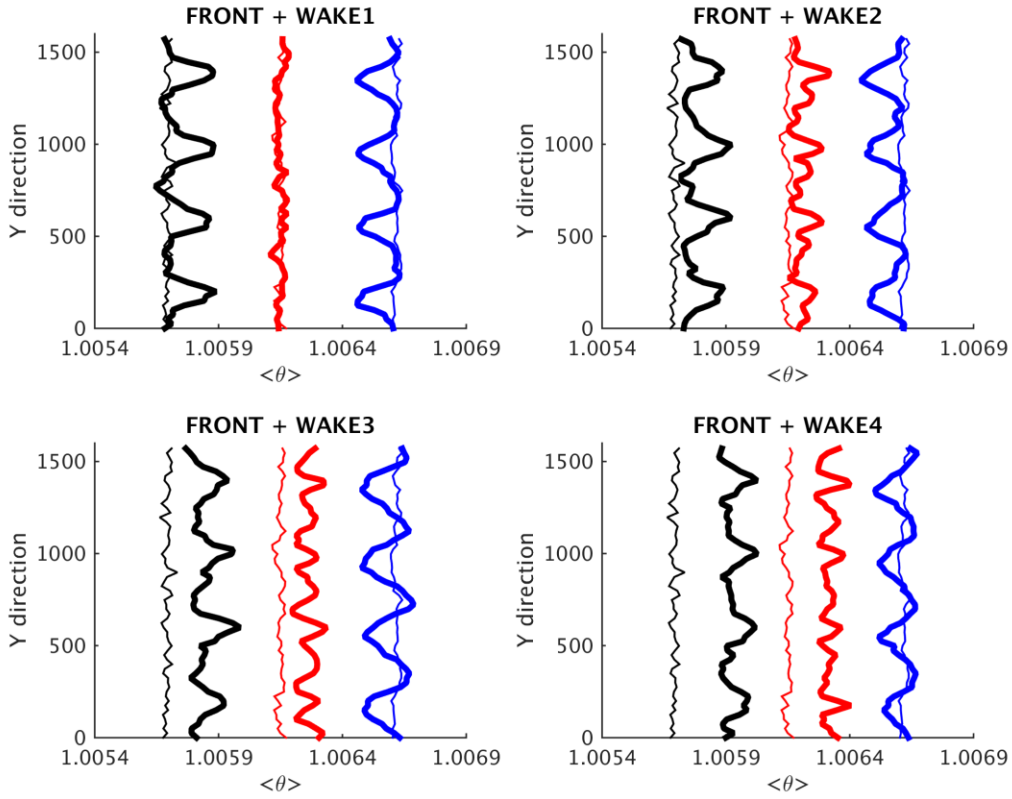

Figure 4.38 Lateral profiles of the temperature for Ct=1.997 for U=6m/s.

Thin line: upstream, bold line: wake at 1.5D. In red at hub height z=100m, in blue above the hub height z=150m and black below the hub height z=50m.

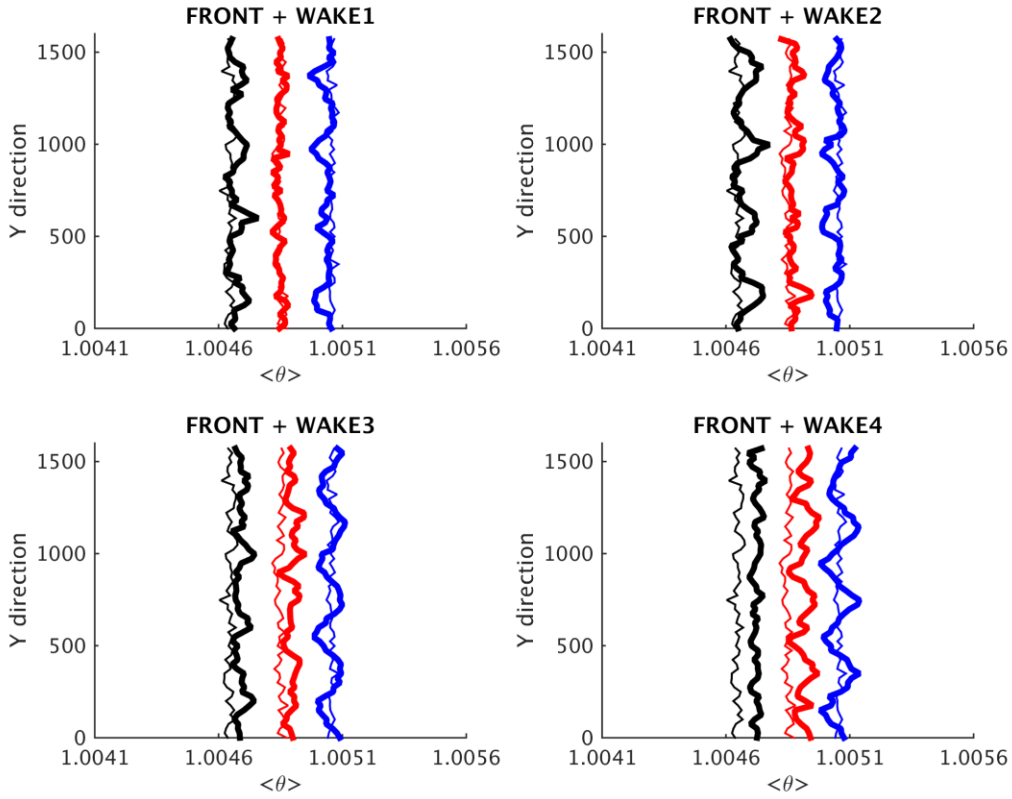

Figure 4.39 Lateral profiles of the temperature for Ct=1.997 for U=8m/s.

Thin line: upstream, bold line: wake at 1.5D. In red at hub height z=100m, in blue above the hub height z=150m and black below the hub height z=50m.

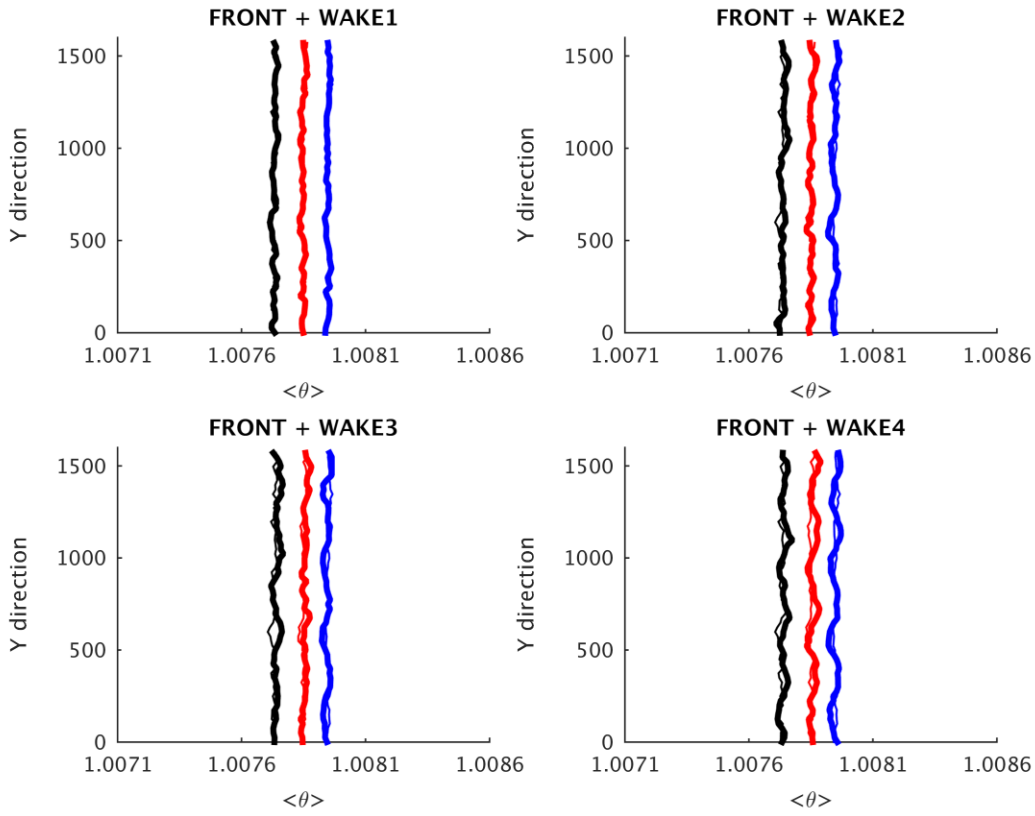

Figure 4.40 Lateral profiles of the temperature for Ct=1.997 for U=10m/s.

Thin line: upstream, bold line: wake at 1.5D. In red at hub height z=100m, in blue above the hub height z=150m and black below the hub height z=50m.

We can remark from the figures above that the temperature at the hub height has a very small variation due to the wake. However, a higher variation of the potential temperature between the upstream and downstream regions can be visible below and above the hub height. The heat is carried with the flow and a mixing between hot (from the previous wake) and cold fluid (from the pinched flow) happens. The curves are squeezed together as we increase the velocity. The variations decrease as we increase the velocity and the variation between the downstream and upstream region increases as we go downstream for each individual case. It gets hotter above the hub height. We can also

remark an overall heating of the wakes and in the vicinity of the wind turbines since the flow from the previous wind turbine is transferred into the next one.

4.8 Humidity profiles:

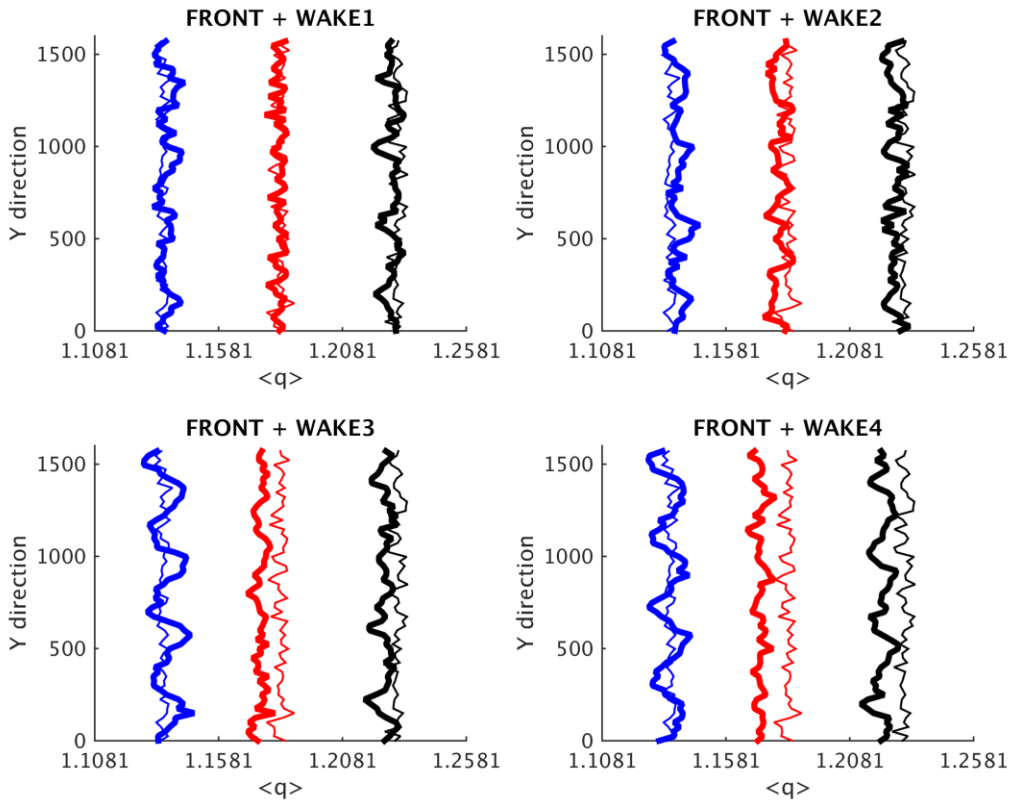

Figure 4.41 Lateral profiles of the humidity for Ct=0.671 for U=6m/s.

Thin line: upstream, bold line: wake at 1.5D. In red at hub height z=100m, in blue above the hub height z=150m and black below the hub height z=50m.

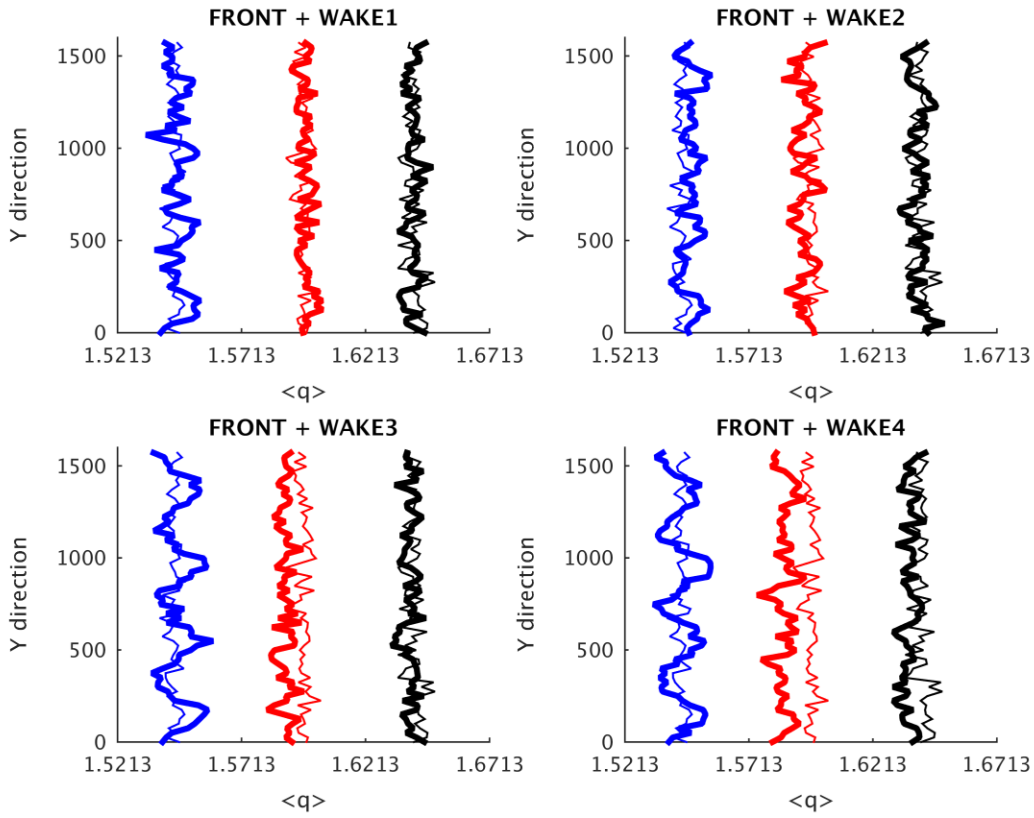

Figure 4.42 Lateral profiles of the humidity for Ct=0.671 for U=8m/s.

Thin line: upstream, bold line: wake at 1.5D. In red at hub height z=100m, in blue above the hub height z=150m and black below the hub height z=50m.

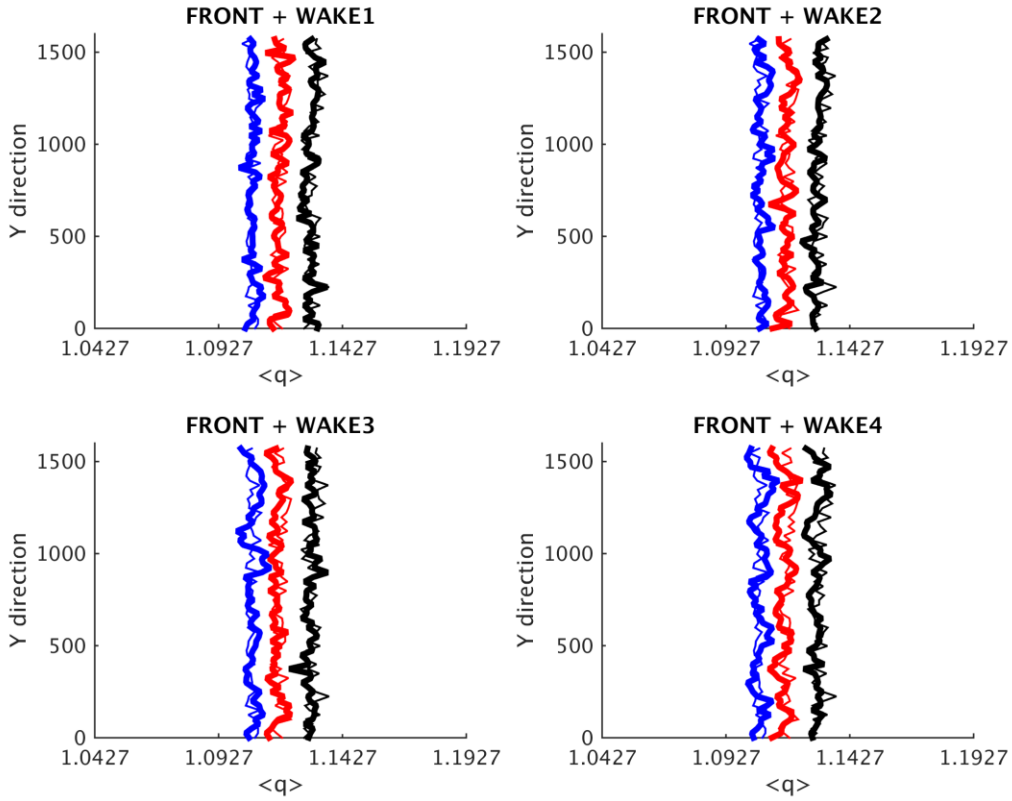

Figure 4.43 Lateral profiles of the humidity for Ct=0.671 for U=10m/s.

Thin line: upstream, bold line: wake at 1.5D. In red at hub height z=100m, in blue above the hub height z=150m and black below the hub height z=50m.

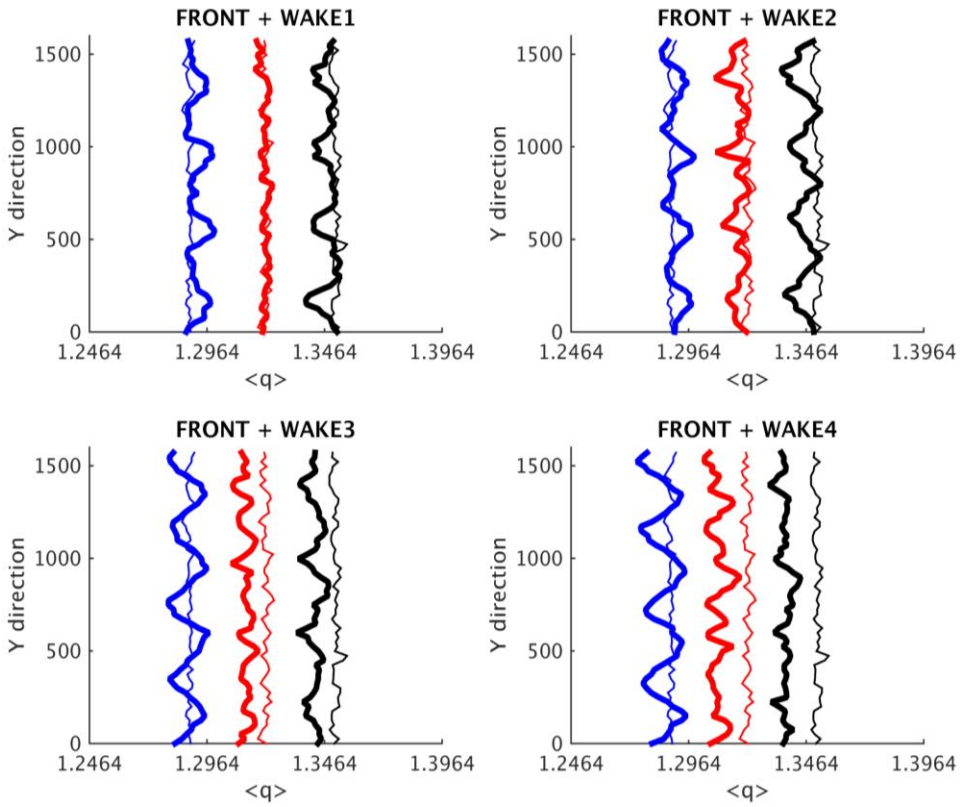

Figure 4.44 Lateral profiles of the humidity for Ct=1.997 for U=6m/s.

Thin line: upstream, bold line: wake at 1.5D. In red at hub height z=100m, in blue above the hub height z=150m and black below the hub height z=50m.

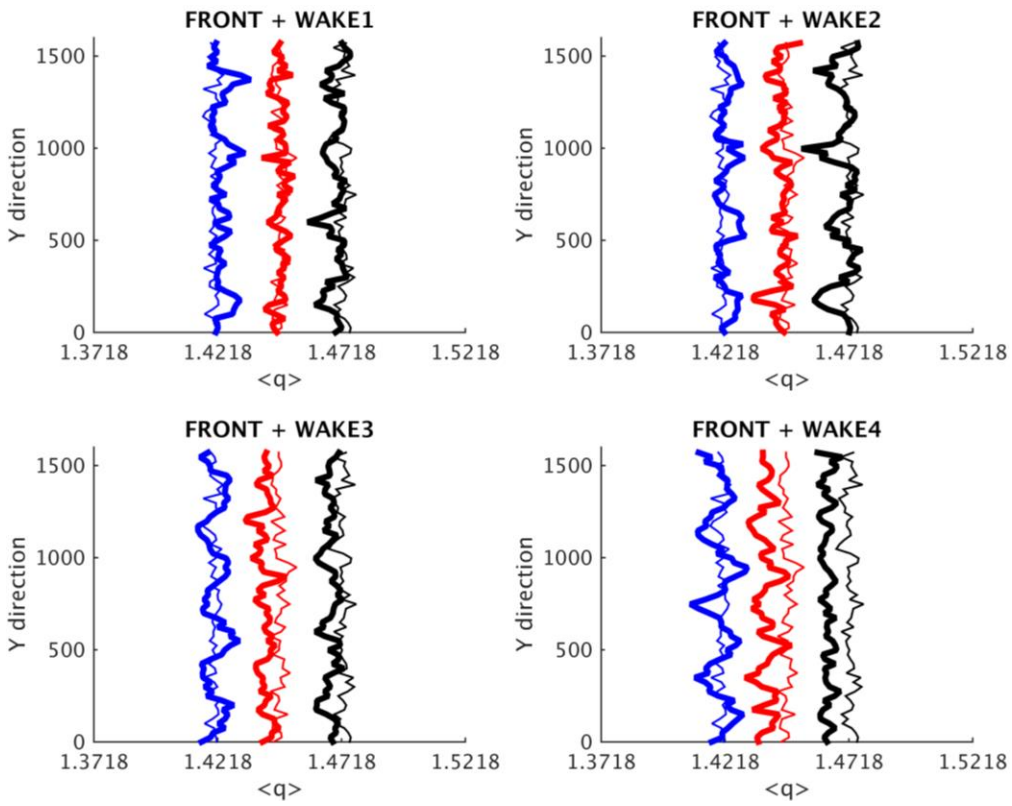

Figure 4.45 Lateral profiles of the humidity for Ct=1.997 for U=8m/s.

Thin line: upstream, bold line: wake at 1.5D. In red at hub height z=100m, in blue above the hub height z=150m and black below the hub height z=50m.

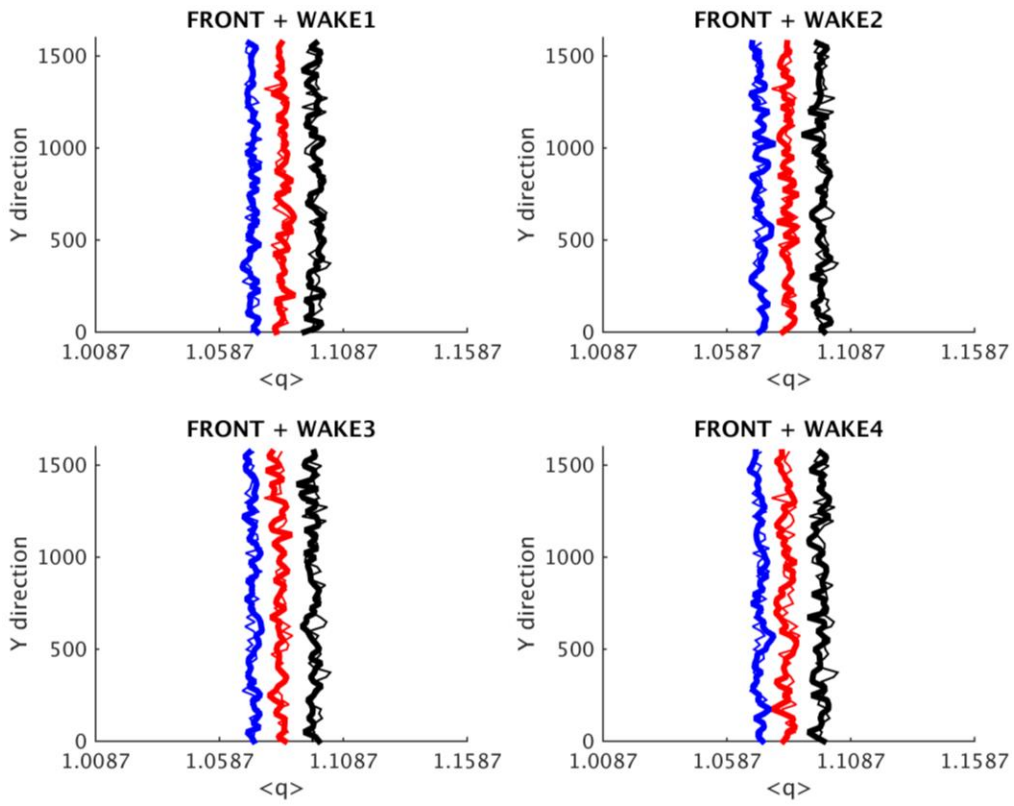

Figure 4.46 Lateral profiles of the humidity for Ct=1.997 for U=10m/s.

Thin line: upstream, bold line: wake at 1.5D. In red at hub height z=100m, in blue above the hub height z=150m and black below the hub height z=50m.

Table 4.4 Variation of the specific humidity for all wind farm cases.

CASES WIND FARM	VARIATION OF SPECIFIC HUMIDITY							
	WT 1		WT 2		WT 3		WT 4	
	B	A	B	A	B	A	B	A
WF1	-1.45%	+1.525%	-1.29%	+0.958%	-1.61%	+1.21%	-1.53%	+1.052%
WF2	-0.75%	+0.49%	-0.56%	+1.027%	-0.56%	+0.587%	-0.65%	+0.49%
WF3	-0.67%	+0.344%	-0.623%	+0.40%	-0.62%	+0.394%	-0.56%	+0.296%
WF4	-0.90%	+0.515%	-1.04%	+1.36%	-1.75%	+1.427%	-2.07%	+1.025%
WF5	-0.88%	+0.813%	-1%	+0.90%	-1.18%	+0.692%	-1.20%	+0.751%
WF6	-0.77%	+0.59%	-0.69%	+0.74%	-0.76%	+1.26%	-0.90%	+0.653%

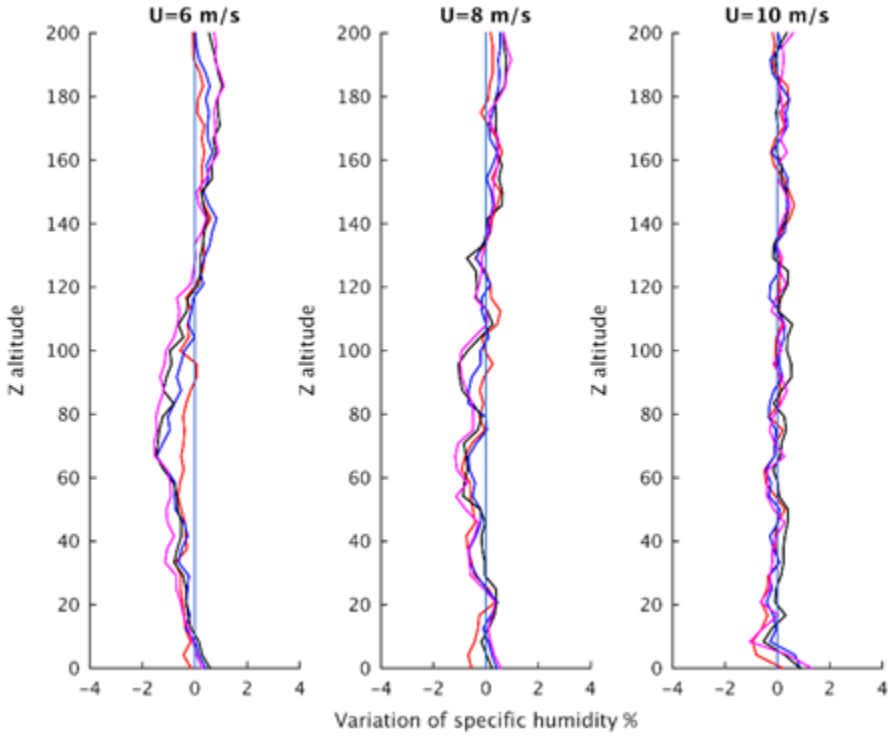

Figure 4.47 Vertical profiles of the variation of the specific humidity for constant Ct=0.761 for different velocities.

In red: 1st wake, blue: 2nd wake, black: 3rd wake and magenta: 4th wake.

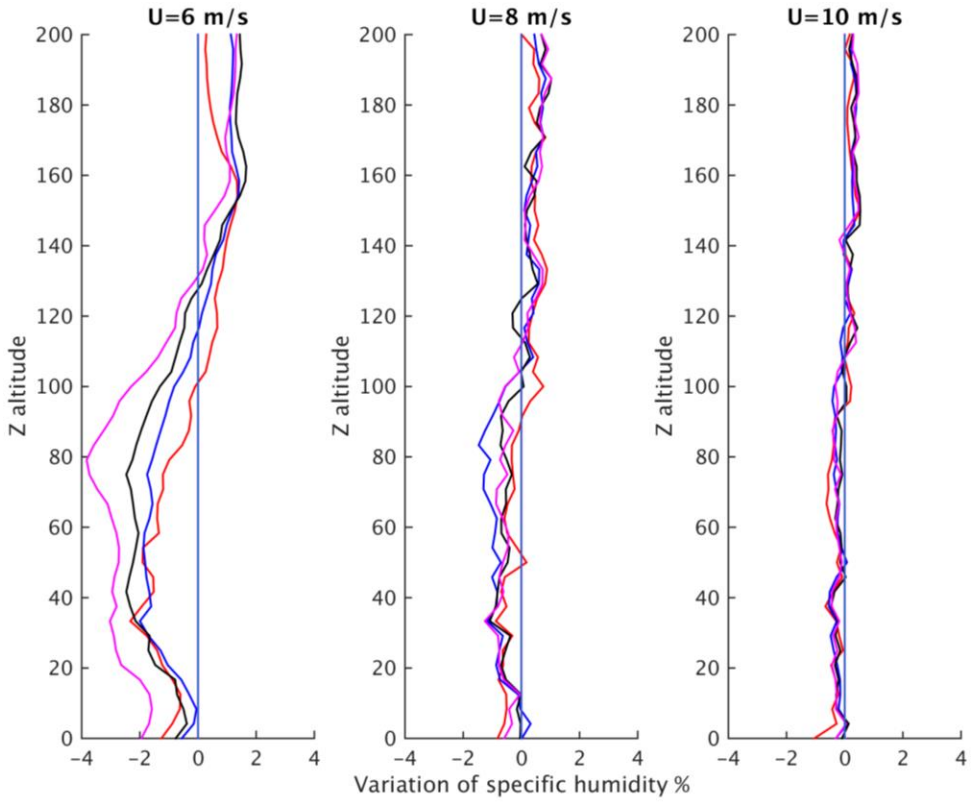

Figure 4.48 Vertical profiles of the variation of the specific humidity for constant Ct=1.997 for different velocities.

In red: 1st wake, blue: 2nd wake, black: 3rd wake and magenta: 4th wake.

For the humidity profile, we will calculate the variation of the specific humidity below and above the wind turbine, since at the hub height we can remark that the variation between the upstream and downstream region is very small and can be negligible. The hub location acts as an inflection point where the behavior below the wind turbine is opposite from above. From figures of the humidity along the lateral direction, we can see that it is less humid as we go downstream in the single wind turbine case. Since the amount of water is not modified, the heated flow from the previous wind turbine is injected in the following one. We can remark from Table 4.4 that as the

velocity increases, the variation of the specific humidity decreases. Below the wind turbine, we can remark that the negative variation decreases as we increase the velocity; the same pattern can be seen above the wind turbine. Along the streamwise direction, we can remark that the specific change is roughly the same for all the successive wind turbines, meaning that the position of the wind turbine does not affect the humidity. The same pattern has been deduced from the case of the single wind turbine.

CHAPTER V

CONCLUSION

A large eddy simulation (LES) investigation has been performed in this thesis to determine the effect of individual wind turbines or wind farms on the specific humidity in the atmospheric boundary layer. To parameterize the wind turbine, the actuator disk model was employed due to grid and computational cost requirements. The numerical tool was a pseudo-spectral incompressible LES algorithm with Adams-Bashforth time-matching integration. The pressure was determined by solving the Poisson equation. Monin-Obhukov similarity theory was used to quantify the momentum, humidity and heat flux at the wall within a wall-modelling framework. The SGS were modeled using a Lagrangian scale-dependent model for scalars. In order to apply realistic turbulence at the inflow, a concurrent precursor simulation method was employed.

Two simulation cases have been studied here: a single wind turbine and a wind farm (4x4 turbines) with different velocities and different thrust coefficients. The simulation results - consisting of contour plots and profiles along the lateral and vertical direction of the instantaneous, time-averaged velocity, specific humidity and potential temperature - showed that the wind turbine slows down, heats the flow and modify the specific humidity distribution with an increase above and a decrease below the wind turbine. Namely, the specific humidity variation is concentrated below and above the hub height of the wind turbines (it remains approximately the same at the hub height) due to

the behavior the flow around the wind turbine. The thrust coefficient has an impact on the velocity, potential temperature and specific humidity: a higher Ct has more effects on the flow than a lower one because it poses more of an obstacle to the flow. The same pattern can be seen in the single wind turbine or wind farm.

A future work will focus on implementing the actuator disk model with rotation to increase the accuracy associated with the effect that a wind turbine wake can have on the atmospheric boundary layer. In addition, the work will focus on finding the optimal positioning of wind turbines in large wind farms in order to increase their efficiency and benefit the agricultural crops located near them.

REFERENCES

1. Albertson, J. D. (1996) Large eddy simulation of land-atmosphere interaction. Ph.D. thesis, 185 pp., Univ. of Calif., Davis.

2. Albertson, J.D., Parlange, M.D., Kiely, G. and Eichinger, W.E. (1996) The average dissipation rate of turbulent kinetic energy in the neutral and unstable atmospheric surface layer, J. Geophys. REs., In Press.

3. Aldama, A.A. (1990) Filtering Techniques for Turbulent Flow Simulation. Lecture Notes in Engineering. Vol 56

4. Andren, A. (1995) The structure of stably stratified atmospheric boundary layers: A large-eddy simulation study, Q. J. R. Meteorol. Soc., 121, pp.961-985

5. Andren, A., Brown A.R., Graf, J., Mason, P.J., Moeng, C.H., Nieuwstad, F.T.M. and Schumann, U. (1994) Large eddy simulation of the neutrally stratified boundary layer: a comparison of four computer codes. Q. J. R. Metl. Soc. 120, 1457-1484.

6. Augstein, E., Riehl, H., Ostapoff, F. and Wagner, V. (1973) Mass and energy transport in an undisturbed Atlantic trade-wind flow, Mon. Weath. Rev., Vol. 101, pp.101-111.

7. Baidya Roy, S. and Traiteur, J. (2010) Impacts of wind farms on surface air temperatures. PNAS, Vol.107, pp.17899-17904

8. Baidya Roy, S., Pacala, S.W. and Walko, R.L. (2004) Can large wind farms affect local meteorology?, Journal of Geophysical Research, Vol.109, pp.375-404.

9. Barrie, D.B. and Kirk-Davidoff, D.B. (2009) Weather response to management of a large wind turbine array, Atmospheric Chemistry and Physics. Discussions, Vol. 9, pp. 2917-2931.

10. Barthelmie, R. J. and Jensen, L. E. (2010) Evaluation of wind farm efficiency and wind turbine wakes at the Nysted offshore wind farm. Wind Energ., 13: 573–586.

11. Barthelmie, R.J., Frandsen, S.T., Hansen, K., Schepers, J.G., Rados, K., Schelz, W., Neubert, A., Jensen, L.E., Neckelmann, S. (2009) Modelling the impact of wakes on power output at Nysted and Horns Rev. In: European Wind Energy Conference, Marseille.

12. Barthelmie, R.J., Frandsen, S.T., Réthoré, P.E., Jensen, L. (2007) Analysis of the atmospheric impacts on the development of wind turbine wakes at the Nysted wind farm. In: European Offshore Wind Conference, Berlin.

13. Betz, A. (1920) Das Maximum der theoretisch moÈ glichen AusnuÈ tzung des Windes durch Windmotoren. Z. Gesamte. Turbinewesen, 26.

14. Bou-Zeid, E., Meneveau, C. and Parlange, M. (2004) Comparison of four eddy viscosity SGS models in Large Eddy Simulation of flows over rough walls. ASME Heat Transfer/Fluids Engineering Summer Conference, Charlotte, North Carolina, USA. July 11-15 2004.

15. Bou-Zeid, E., Meneveau, C. and Parlange, M.B. (2005) A scale dependent Lagrangian dynamic model for large eddy simulation of complex turbulent flows. Physics of Fluids, 17

16. Burton, T., Sharpe, D., Jenkins, N. and Bossanyi, E. (2001) Wind Energy Handbook. Wiley, New York.

17. Businger, J., Wyngaard, J., Izumi, Y. and Bradley, E. (1971) Flux profile relationships in the atmospheric surface layer. J. Atmos. Sci., 28, pp.181-189.

18. Cabezon, D., Migoya, E. and Crespo, A. (2011) Comparison of turbulence models for the computational fluid dynamics simulation of wind turbine wakes in the atmospheric boundary layer. Wind Energy 14, 909-921.

19. Calaf, M., Meneveau, C. and Meyers, J. (2010) Large eddy simulation study of fully developed wind turbine array boundary layers. Phys. Fluids 22, 015110.

20. Calaf, M., Parlange, M.B. and Meneveau, C. (2011) Large eddy simulation study of scalar transport in fully developed wind-turbine array boundary layers. Phys. Fluids 23, 126603.

21. Canuto, C., Hussaini, M. Y., Quarteroni, A. and Zang, T. A. (1988) Spectral Methods in Fluid Dynamics. Springer.

22. Chamorro, L.P. and Porté-Agel, F. (2009) A Wind-Tunnel Investigation of Wind-Turbine Wakes: Boundary-Layer Turbulence Effects. Boundary-Layer Meteorol (2009) 132: 129.

23. Chamorro, L.P. and Porté-Agel, F. (2011) Turbulent flow inside and above a wind farm: a wind tunnel study. Energies 4, 1916-1936.

24. Clark, R.H., Dyer, A.J., Brook, R.R., Reid, D.G. and Troup, A.J. (1971) The Wangara experiment: Boundary layer data. Tech. Paper 19, Div. Meteor. Phys. CSIRO, Australia.

25. Cleijine, J.W. (1993) Results of the Sexbierum Wind Farm Single Wake Measurements. Technical Report TNO-93-082, TNO Institute of Environmental and Energy Technology, The Netherlands.

26. Coleman, C.N., Ferzinger, J.H. and Spalart, P.R. (1992) Direct simulation of the stably stratified turbulent Ekman layer, J. Fluid Mech., 244, pp.677-712.

27. Crespo, A. and Hernández, J. (1996) Turbulence characteristics in wind-turbine wakes. J. Wind Eng. Ind. Aerodyn. 61, 71.

28. Deardorff, J.W. (1970) A numerical study of three-dimensional turbulent channel flow at large Reynolds numbers. Journal of Fluid Mechanics. 41 (2): 453–480.

29. Deardorff, J.W. (1972) Numerical investigation of neutral and unstable planetary boundary layers, J. Atmos. Sci, Vol. 29, pp.91-115.

30. Deardorff, J.W. (1973) Three-dimensional numerical study of the height and mean structure of a heated planetary boundary layer, Boundary-Layer Meteorology, Vol. 7, pp.81-106.

31. Derbyshire, S.H. (1995) Stable Boundary layers: observations, models and variability part 1: modelling and measurements. 74:19.

32. Elliot, D.L. (1991) Status of wake and array loss research. In: Windpower Conference, Palm Springs, California.

33. Garratt, J.R. (1992) The atmospheric boundary layer. Cambridge University Press. pp. 316.

34. Germano, M., Piomelli, U., Moin, P., and Cabot, W. (1991) A dynamic subgrid-scale eddy viscosity model. Physics of Fluids A, 3 (7), pp. 1760-1765.

35. Ghosal, S., Lund, T.S., Moin, P. and Akselvoll, K. (1995) A dynamic localization model for large eddy simulation of turbulent flows. J. of Fluid Mech. Vol 286. P229-255.

36. Grindstein, F.F., Margolin, L.G. and Rider, W.J. (2007) Implicit Large Eddy Simulation: Computing Turbulent Fluid Dynamics, 1st ed. Cambridge University Press, Cambridge.

37. Hadfield, M.G., Cotton, W.R. and Pielke, R.A. (1991) Large-eddy simulations of thermally forced circulations in the convective boundary layer. Part I: A small-scale circulation with zero wind. Bound.-Layer Meteor. 57. 79-114.

38. Haworth, D.C. and Jansen, K. (2000) Large-eddy simulation on unstructured deforming meshes: towards reciprocating IC engines. Comput. Fluids 29, 493

39. Haywood, J. and Sescu, A. (2015) Large eddy simulation study of moving objects in thermally-stratified boundary layer flows.

40. Hechtel, L.M., Moeng, C.H. and Stull, R.B. (1990) The effects of nonhomogeneous surface fluxes on the convective boundary layer: A case study by large-eddy simulation. J. Atmos. Sci. 47. 1721-1741.

41. Henschen, M., Demchak, K., Herrholtz, B., Rudkin, M., Rhudy, L., Larson, E., Doogs, B., Holland, J., and J. Martin (2011) Do wind turbines affect weather conditions? A case study in Indiana. Journal of Purdue Undergraduate Research, 1, 22-29.

42. Ivanell, S. (2009) Numerical Computations of Wind Turbine Wakes (Ph.D. thesis), Department of Mechanics, Royal Institute of Technology, Stockholm, Sweden.

43. Ivanova, L.A. and Nadyozhina, E.D. (1998) Wind flow deformation inside the wind farm, Journal of Wind Engineering and Industrial Aerodynamics, Vol. 74-76, pp. 389-397.

44. Jensen, L.E., Morch, C., Sorensen, P.B. and Svendsen, K.H. (2004) Wake Measurements from the Horns Rev Wind Farm. In: European Wind Energy Conference, London.

45. Jimenez, A., Crespo, A., Migoya, E. and Garcia, J. (2008) Large-eddy simulation of spectral coherence in a wind turbine wake Environmental Research Letters, Volume 3, Number 1.

46. Keith, D.W., Decarolis, J.F., Denkenberger, D.C., Lenschow, D.H., Malyshev, S.L., Pacala, S. and Rasch, P.J. (2004) The influence of large-scale wind power on global climate, Proceedings of National Academy of Science, Vol. 101, pp. 16115-16120.

47. Lanchester, F.W. (1915) A contribution to the theory of propulsion and the screw propeller. Trans. Inst. Naval Archit., 57.

48. Lee, S., Churchfield, M.J., Moriarty, P.J., Jonkman, J. and Michalakes, J. (2013) A Numerical Study of Atmospheric and Wake Turbulence Impacts on Wind Turbine Fatigue Loadings, Journal of Solar Energy Engineering, Vol. 135, pp.031001.

49. Leonard, A. (1974) Energy cascade in large eddy simulation of turbulent fluid flows. Adv. Geophys. 18,237-248

50. Lilly, D.K. (1967) The representation of small scale turbulence in numerical simulation experiments. Proc. IBM Scientific Computing Symposium on Environmental Sciences, p. 195.

51. Lu, H., and Porte-Agel, F. (2013) Large-eddy simulation of a very large wind farm in a stable atmospheric boundary layer. Phys. Fluids, 23, 065 101.

52. Ma, J., Wang, F. and Tang, X. (2009) Comparison of Several Subgrid-Scale Models for Large-Eddy Simulation of Turbulent Flows in Water Turbine. Fluid Machinery and Fluid Mechanics: 4th International Symposium (4th ISFMFE) 328-334

53. Mason, P.J. (1989) Large-eddy simulation of the convective atmospheric boundary layer. J. Atmos. Sci. 46. 1492-1516.

54. Mason, P.J. and Thompson, D.J. (1987) Stochastic backscatter in large-eddy simulation of boundary layers, J. Fluid Mech., 242, pp.51-78

55. Mason, P.J., and Derbyshire, S.H. (1990) Large-eddy simulation of the stably-stratified atmospheric boundary layer, Boundary-Layer Meteorol., Vol. 53, pp.117.

56. Meyers, J. and and Meneveau, C. (2010) Large Eddy Simulations of large wind-turbine arrays in the atmospheric boundary layer AIAA Paper 2010-827.

57. Mehta, D., van Zuijlen, A.H., Koren, B., Holierhoek, J.G. and Bijl, H. (2014) Large Eddy Simulation of wind farm aerodynamics: A review. J. Wind Eng. Ind. Aerodyn. Vol. 133. pp.1-17

58. Meneveau, C. (2010) Turbulence: Subgrid-Scale Modeling. Scholarpedia, 5(1):9489.

59. Meneveau, C., Lund, T., and Cabot, W. (1996) A Lagrangian dynamic subgrid-scale model of turbulence. J. of Fluid Mechanics, Vol 319, pp. 353-385.

60. Moeng, C.H. (1984) A large Eddy simulation model for the study of planetary boundary-layer turbulence. J. Atmosph. Sci. 41(13), 2052-2062

61. Moeng, C.H. (1986) Large Eddy Simulation of a Stratus-Topped Boundary Layer. Part II: Implications for Mixed-Layer Modeling.

62. Moeng, C.H. and Wyngaard, J.C. (1984) Statistics of conservative scalars in the convective boundary layer. J. Atmos. Sci. 41. 3161-3169.

63. Moin, P., Squires, K., Cabot, W. and Lee, S. (1991) A dynamic subgrid-scale model for compressible turbulence and scalar transport. Phys. of Fluids A 3 (11), 2746–2757.

64. Monin, A.S. and Obukhov, A.M. (1954) Basic laws of turbulent mixing in the surface layer of the atmosphere, Tr. Akad. Nauk SSSR Geofiz. Inst, Vol. 24, pp.163-187.

65. Nicoud, F. and Ducros, F. (1999) Subgrid-Scale Stress Modelling Based on the Square of the Velocity Gradient Tensor. F. Flow, Turbulence and Combustion 62: 183.

66. Nieuwstadt, F. T. M. (1992) A Large Eddy simulation if a line source in a convective atmospheric boundary layer-I. dispersion characteristics. Atm. Env., 26A, 485-495.

67. Obukhov, A.M. (1971) Turbulence in an atmosphere with a non-uniform temperature (English Translation), Boundary-Layer Meteorology, Vol. 2, pp.7-29.

68. Okulov, V.L. and van Kuik, G.A.M. (2011) The Betz–Joukowsky limit: on the contribution to rotor aerodynamics by the British, German and Russian scientific schoolsŽ. J. Wind Energ.

69. Panofsky, H. and Dutton, J. (1984) Atmospheric Turbulence: Models and Methods for Engineering Applications. John Wiley & Sons, New York.

70. Piomelli, U. and Balaras, E. (2002) Wall-layer models for large-eddy simulations. Annual Rev. Fluid Mech. 34, 349-374.

71. Pope, S.B. (2000) Turbulent Flows. Cambridge University Press, Cambridge.

72. Porté-Agel, F.,Wu, Y.-T., Lu, H. and Conzemius, R. (2011) Large-eddy simulation of atmospheric boundary layer flow through wind turbines and wind farms. J. Wind Eng. Ind. Aerodyn. 99. 154-168.

73. Porté-Agel, F., Lu, H., Wu, Y.-T. (2014) Interaction between large wind farms and the atmospheric boundary layer. Proc. IUTAM 10, 307-318.

74. Porté-Agel, F., Meneveau, C. and Parlange, M.B. (2000) A scale-dependent dynamic model for large-eddy simulation: application to a neutral atmospheric boundary layer. J. Fluid Mech. 415, 261.

75. Q3 Report : American Wind Energy Third Quarter Market Report" (17 October 2012). AWEA.

76. Rajewski, D.A. (2013) CWEX (Crop/Wind-Energy Experiment): Measurements of the interaction between crop agriculture and wind power. Iowa State University.

77. Sagaut, P. (2006) Large Eddy Simulation for Incompressible Flows, 3rd ed. Springer-Verlag, Berlin.

78. Schmidt, H., and Schumann, U. (1989) Coherent structure of the convective boundary layer derived from large-eddy simulations. J. Fluid Mech. 200. 511-562.

79. Smith, C., Barthelmie, R. and Pryor, S. (2011) In situ observations of the influence of a large onshore wind farm on near-surface temperature, turbulence intensity and wind speed profiles. Environ. Res. Lett., 8, 034 006.

80. Schumann, U. (1988) Minimum friction velocity and heat transfer in the rough surface layer of a convective boundary layer. Boundary-Layer Meteorol. 44. 311-326.

81. Schumann, U. (1996) Direct and large eddy simulation of stratified homogeneous shear flows. Dyn. Atmos. Oceans 23. 81-98.

82. Sescu, A. and Meneveau, C. (2013) A control algorithm for statistically stationary large-eddy simulations of thermally stratified boundary layers, Quart. J. Roy. Meteorol. Soc.

83. Sescu, A. and Meneveau, C. (2015) Large Eddy Simulation and single column modeling of thermally-stratified wind turbine arrays for fully developed, stationary atmospheric conditions. Journal of Atmospheric and Oceanic Technology,

84. Shaw, R.H. and Schumann, U. (1992) Large-eddy simulation of turbulent flow above and within a forest. Boundary-Layer Meteorol. 61. 47-64.

85. Smagorinsky, J. (1963) General circulation experiments with the primitive equations, i. the basic experiment. Monthly Weather Review. 91. Pp.99-164.

86. Sorbjan, Z. (1989) Structure of the Atmospheric Boundary Layer. Prentice Hall, New Jersey.

87. Sorbjan, Z. (2005) Local Structure of Turbulence in Stably Stratified Boundary Layers. J. of Atmos. Sciences. Vol 63.

88. Sorbjan, Z. (1995) Toward Evaluation of Heat Fluxes in the Convective Boundary Layer. J. Appl. Meteorol. 34. 1565-1583

89. Stevens, R., Graham, J. and Meneveau, C. (2014) A concurrent precursor inflow method for Large Eddy Simulations and applications to finite length wind farms, Renewable Energy. Vol. 68. pp. 46-50.

90. Stoll, R. and Porté-Agel, F. (2006) Dynamic subgrid-scale models for momentum and scalar fluxes in large-eddy simulations of neutrally stratified atmospheric boundary layers over heterogeneous terrain. Water Resour. Res. 42, W01409.

91. Stull, R.B. (1998) An Introduction to Boundary Layer Meteorology. Kluwer Academic Publishers, Dordrecht, The Netherlands.

92. Sullivan, P.P., McWilliams, J.C. and Moeng, C-H. (1994) A subgrid scale model for large eddy simulation of planetary boundary layer flows. Journal Boundary-Layer Meteorology. pp. 71- 247.

93. Sullivan, P.P., McWilliams, J.C. and Moeng, C-H. (1996) A grid nesting method for large eddy simulation of planetary boundary layer flows. Journal Boundary-Layer Meteorol. Pp.80-167.

94. Tabor, G.R. and Baba-Ahmadi, M.H. (2010) Inlet conditions for large eddy simulation: A review. Computers & Fluids.Vol. 39 pp.553-567.

95. Tao, B., Katz, J. and Meneveau, C. (2002) Statistical geometry of subgrid-scale stresses determined from holographic particle image velocimetry measurements. J.Fluid Mechanics, 457, pp. 35-78

96. Taylor, G.J. (1990) Wake Measurements on the Nibe Wind Turbines in Denmark. Technical Report CEC contract EN3W0039UK, UK National Power.

97. van Haren, L. and Nieuwstadt, F. T. M. (1989) The Behavior of Passive and Buoyant Plumes in a Convective Boundary Layer, as Simulated with a Large-Eddy Model. J. Appl. Meteor. 28. 818–832.

98. Vermeer, L.J., Sorensen, J.N. and Crespo, A. (2003) Wind turbine wake aerodynamics. Prog. Aerosp. Sci. 39, 467.

99. Vreman, A. W. (2004) An eddy-viscosity subgrid-scale model for turbulent shear flow: algebraic theory and applications. Physics of Fluids 16 (10), 3670–368.

100. Walko, R. L., Cotton, W. R. and Pielke, R.A. (1992) Large eddy simulation of the effects of hilly terrain on the convective boundary layer. Bound. Layer. Meteor. 58. 133-150.

101. Wharton, S., and Lundquist, J.K. (2012) Atmospheric stability affects wind turbine power collection. Environmental Research Letters. Vol.7

102. Wyngaard, J.C. (2010) Turbulence in the Atmosphere. Pennsylvania State University. MAHRT

103. Wyngaard, J.C. and Brost, R.A. (1984) Town-down and bottom-up diffusion of a scalar in the convective boundary layer. J. Atmos. Sci.41. Pp.102-112.

104. Wu, Y.-T., and Porte-Agel, F. (2011) Large-eddy simulation of wind turbine wakes: Evaluation of turbine parameterization. Boundary-Layer Meteorol, 138, 345.

105. Zhang, W., Markfort, C. and Porte-Agel, F. (2013) Experimental study of the impact of large-scale wind farms on land-atmosphere exchanges. Environ. Res. Lett., 8, 1–8.